Monthly Notices
of the
ROYAL ASTRONOMICAL SOCIETY

Mon. Not. R. Astron. Soc. **416,** 2318–2340 (2011) doi:10.1111/j.1365-2966.2011.19206.x

Limits on the local dark matter density

Silvia Garbari,[1⋆] Justin I. Read[2,3] and George Lake[1]

[1]*Institute of Theoretical Physics, University of Zürich, Winterthurerstrasse 190, 8057 Zürich, Switzerland*
[2]*Department of Physics and Astronomy, University of Leicester, University Road, Leicester LE1 7RH*
[3]*Institute for Astronomy, Department of Physics, ETH Zürich, Wolfgang-Pauli-Strasse 27, CH-8093 Zürich, Switzerland*

Accepted 2011 June 7. Received 2011 May 30; in original form 2011 March 8

ABSTRACT

We revisit systematics in determining the local dark matter density $\rho_{\rm dm}$ from the vertical motion of stars in the solar neighbourhood. Using a simulation of a Milky Way like galaxy, we determine the data quality required to detect $\rho_{\rm dm}$ at its expected local value. We introduce a new method for recovering $\rho_{\rm dm}$ that uses moments of the Jeans equations, combined with a Markov chain Monte Carlo technique, to marginalize over the unknown parameters. Given sufficiently good data, we show that our method can recover the correct local dark matter density even in the face of disc inhomogeneities, non-isothermal tracers and a non-separable distribution function. We illustrate the power of our technique by applying it to *Hipparcos* data. We first make the assumption that the A- and F-star tracer populations are isothermal. This recovers $\rho_{\rm dm} = 0.003^{+0.009}_{-0.007}\,{\rm M}_\odot\,{\rm pc}^{-3}$ ($\rho_{\rm dm} = 0.11^{+0.34}_{-0.27}\,{\rm GeV\,cm}^{-3}$, with 90 per cent confidence), consistent with previous determinations. However, the vertical dispersion profile of these tracers is poorly known. If we assume instead a non-isothermal profile similar to that of the blue disc stars from SDSS DR-7 recently measured, we obtain a fit with a very similar χ^2 value, but with $\rho_{\rm dm} = 0.033^{+0.008}_{-0.009}\,{\rm M}_\odot\,{\rm pc}^{-3}$ ($\rho_{\rm dm} = 1.25^{+0.30}_{-0.34}\,{\rm GeV\,cm}^{-3}$ with 90 per cent confidence). This highlights that it is vital to measure the vertical dispersion profile of the tracers to recover an unbiased estimate of $\rho_{\rm dm}$.

Key words: Galaxy: disc – Galaxy: kinematics and dynamics – Galaxy: structure – dark matter.

1 INTRODUCTION

There are two approaches to determine the local dark matter density: extrapolating its value from the Milky Way's (MW's) rotation curve ($\rho_{\rm dm,ext}$; e.g. Sofue, Honma & Omodaka 2009; Weber & de Boer 2010); and using the kinematics of stars in the solar neighbourhood ($\rho_{\rm dm}$; e.g. Oort 1932, 1960). The first requires an assumption about the global and local shapes of the dark matter halo. Simple extrapolations that assume spherical symmetry find $\rho_{\rm dm,ext} \simeq 0.01\,{\rm M}_\odot\,{\rm pc}^{-3}$ (Sofue et al. 2009). However, uncertainties about the halo shape lead to errors of at least a factor of 2 (Weber & de Boer 2010). Even larger uncertainties arise if the MW has a dark matter disc (Lake 1989; Read et al. 2008) as predicted by recent cosmological simulations. The second approach relies on fewer assumptions, and this is our focus in this paper. However, both approaches are complementary and, together, provide a powerful probe of Galactic structure. If $\rho_{\rm dm} < \rho_{\rm dm,ext}$, this suggests a prolate dark matter halo for the MW, while $\rho_{\rm dm} > \rho_{\rm dm,ext}$ could imply either an oblate halo or a dark matter disc (Lake 1989; Read et al. 2008, 2009).

The local dark matter density is needed for direct dark matter search experiments. In the simplest case where the dark matter is a weakly interacting massive particle (WIMP; Jungman et al. 1996; Baudis 2006), these experiments produce results that are degenerate between the WIMP interaction cross-section and the local matter density (Gaitskell 2004; Aprile, Giboni & Majewski 2005; CDMS Collaboration 2008). Thus, extracting WIMP properties requires the knowledge of $\rho_{\rm dm}$ (e.g. Gaitskell 2004).

To date, most limits on WIMP properties have assumed the 'standard halo model' (SHM) density: $\rho_{\rm dm}({\rm R}_\odot) = 0.3\,{\rm GeV\,cm}^{-3}$ ($\simeq 0.008\,{\rm M}_\odot\,{\rm pc}^{-3}$; Jungman et al. 1996).[1] This is similar to the latest rotation curve extrapolated values that assume a spherical MW halo. However, if the MW halo is oblate, or there is a dark matter disc, then this could be a significant underestimate (e.g. Weber & de Boer 2010).

Measuring the local matter and dark matter density from the kinematics of solar neighbourhood stars has a long history dating back to Oort (Oort 1932, 1960) who determined the total matter density $\rho_{\rm tot}({\rm R}_\odot)$. Many studies since then have revisited the determination of both $\rho_{\rm tot}$ and $\rho_{\rm dm}$; we summarize recent results from the literature in Fig. 1.

⋆E-mail: silvia@physik.uzh.ch

[1] $1\,{\rm GeV\,cm}^{-3} \simeq 0.026\,3158\,{\rm M}_\odot\,{\rm pc}^{-3}$. The SHM is an isothermal sphere model for the MW's dark matter halo with a value of the dark matter velocity dispersion assumed to be $\sigma_{\rm iso} \simeq 270\,{\rm km\,s}^{-1}$.

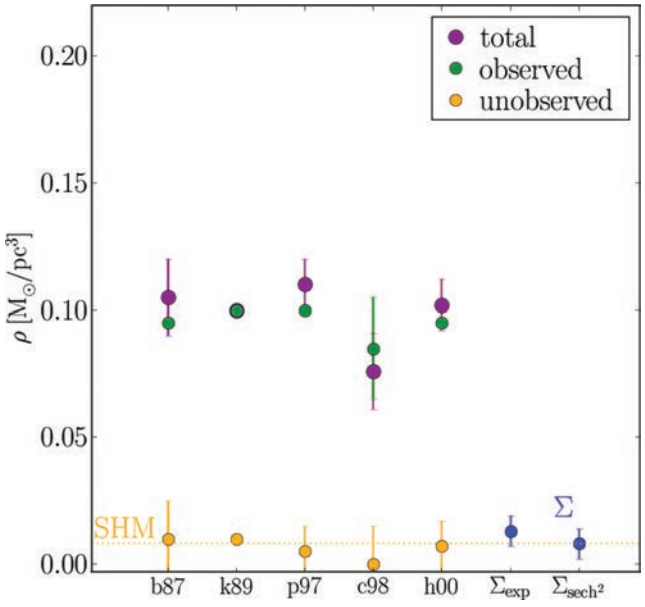

Figure 1. A summary of recent determinations of the total density $\rho_{\rm tot}$ (purple), dark matter density $\rho_{\rm dm}$ (yellow) and observed matter density (green) from the kinematics of solar neighbourhood stars in the literature. The yellow dotted line represents the dark matter density in the SHM. The blue points are the values of $\rho_{\rm dm}$ calculated from the local surface density (using an exponential and a sech^2 profile for the disc; see footnote 2). Data are taken from: b87 – Bienayme, Robin & Creze (1987); k89 – Kuijken & Gilmore (1989a); p97 – Pham (1997); c98 – Creze et al. (1998); and h00 – Holmberg & Flynn (2000). [Correction added after online publication 2011 September 12: figure amended.]

We can see from Fig. 1 that results have converged on no or very little disc dark matter.[2] In addition to the local volume density, several studies have measured the dynamical *surface density* of all gravitating matter – $\Sigma_{{\rm tot},L}$ – rather than the volume density, typically probing up to heights of about $L \sim 1$ kpc above the Galactic disc (e.g. Kuijken & Gilmore 1991; Holmberg & Flynn 2004). If we assume a constant dark matter density over this range, we can estimate the local volume density as $\rho_{\rm dm} = (\Sigma_{{\rm tot},L} - \Sigma_{{\rm s},L})/L$. This gives[3] $\rho_{\rm dm} = 0.013 \pm 0.006\,{\rm M}_\odot\,{\rm pc}^{-3}$ for an exponential and $\rho_{\rm dm} = 0.008 \pm 0.006\,{\rm M}_\odot\,{\rm pc}^{-3}$ for a sech^2 disc profile [correction added after online publication 2011 September 12: $\rho_{\rm dm}$ values amended].

The uncertainties on $\rho_{\rm tot}$ and $\rho_{\rm dm}$ quoted in Fig. 1 owe only to the sample size and observational errors. With current/future surveys like *GAIA* (Jordan 2008; Bailer-Jones 2008), RAVE (Steinmetz 2003; Steinmetz et al. 2006; Zwitter et al. 2008) and SEGUE (Yanny et al. 2009), we expect a dramatic improvement in the number of precision astrometric, photometric and spectroscopic measurements. With this explosion in data, it is timely to revisit the systematic errors in determining $\rho_{\rm dm}$ from solar neighbourhood stars since these will become the dominant source of error, if they are not already. This is the goal of this paper.

Previous work in the literature has examined some of the possible systematics. Statler (1989) approximated the Galactic potential with a Stäckel potential (Stäckel 1895) and used the analytic third integral to treat cross-terms in the Jeans equations. He applied this method to artificial data, superficially resembling data available at the time, finding that systematic uncertainties were at least 30 per cent, due mainly to the sample size and uncertainties in the rotation curve. Kuijken & Gilmore (1989b) reconsidered the determination of the volume density near the Sun with particular emphasis on possible systematic effects in the analyses of local F and K stars. They focused on the importance of modelling the velocity distribution of the stars near the plane (important for their method that assumes that the distribution function is separable; see Section 2) and determining the density distribution as a function of height z above the plane.

In this paper, we study systematic errors using high-resolution N-body simulations. We first build an equilibrium N-body model approximating the MW that satisfies all of the usual assumptions made in determining $\rho_{\rm dm}$ – vertical isotropy in the velocity distribution, separability of the Galactic potential, constant local dark matter density and negligible radial gradient in the tilt of the velocity ellipsoid. We then evolve the disc over several dynamical times to form an inhomogeneous and complex disc structure that includes a strong bar and spiral waves similar to the MW (Drimmel & Spergel 2001; Dehnen 2002; Binney & Tremaine 2008). This breaks many of the usual assumptions, providing a stringent test of different techniques. We first use our simulation to test a standard method in the literature for recovering $\rho_{\rm dm}$. We then present and test a new method that (i) relies only on a 'minimal' set of assumptions; and (ii) uses a Markov chain Monte Carlo (MCMC) technique to marginalize over unknown parameters. The former makes the method – given good enough data – robust to model systematics. The latter allows us to cope with incomplete or noisy data and model degeneracies. Finally, we apply our new method to data from the literature to obtain a new measure of both $\rho_{\rm tot}$ and $\rho_{\rm dm}$.

This paper is organized as follows. In Section 2, we review the basic equations of the method and the assumptions used in past work. We present two methods that we test in detail: the 'HF' method proposed by Fuchs & Wielen (1993) and developed by Holmberg & Flynn (2000); and a new more general method that assumes only equilibrium. In Section 3, we describe the simulation that we use to test these two methods and we confront the different methods with our simulated MW to assess the systematic uncertainties. In Section 4, we apply our new method to data from the literature

[2] We should be careful about what we mean by the terms 'local dark matter' and 'dark matter disc'. In simulations, the dark matter disc has a scaleheight of ∼1–2 kpc (Read et al. 2008), but most importantly, it is just intermediate between the disc ($z_0 \sim 250$ pc) and the halo which has an effective scaleheight of ∼R$_\odot$. Here, we use 'local dark matter' to mean the dark matter within a local volume probed by the motions of stars in the solar neighbourhood. Since this will only probe $\rho_{\rm dm}$ to $|z| \sim 1$ kpc, we can only separate a dark disc from a dark halo using another estimate of the dark matter halo's density. In the past, studies have talked about the 'disc dark matter' to mean the dark matter with a scaleheight similar to that of the stellar disc. Here, we would consider that to be just normalizing our stellar mass distribution rather than being a dark matter component.

[3] We derive the surface density of the visible matter at L as $\Sigma_{{\rm s},L} = \Sigma_{{\rm thin},L} + \Sigma_{{\rm thick},L}$, where

$$\Sigma_{i,L} = 2\int_0^L \rho_i(0) F(z) {\rm d}z$$

with i = thin and thick – for the thin and thick discs, respectively – and $F(z) = \exp(-z/z_{0,i})$ or ${\rm sech}^2(z/z_{{\rm s}})$ if we consider an exponential or sech^2 disc, respectively. The densities at the mid-plane, $\rho_i(0)$, are taken from Table 4 and the exponential (sech^2) disc scaleheights $z_{0,i}$ ($z_{{\rm s},i}$) are calculated from the values in Table 2. The cited values of $\rho_{\rm dm}$ are obtained from a simple average of $\rho_{\rm dm}$ obtained using the dynamical $\Sigma_{\rm tot}$ from Kuijken & Gilmore (1991) and Holmberg & Flynn (2004).

to determine more realistic errors on the local dark matter density. Finally, in Section 5, we present our conclusions.

2 DETERMINING THE LOCAL DARK MATTER DENSITY

Ideally, we should solve the Vlasov–Poisson equations to obtain the gravitational potential Φ from the distribution function of stars $f(\boldsymbol{x}, \boldsymbol{v})$:

$$\frac{\partial f}{\partial t} + \nabla_x f \boldsymbol{v} - \nabla_v f \nabla_x \Phi = 0, \tag{1}$$

$$\nabla^2 \Phi = 4\pi G \rho_{\rm tot}, \tag{2}$$

where G is the gravitational constant, $\rho_{\rm tot}$ is the *total* matter density and the density of tracers ν follows from the distribution function: $\nu = \int {\rm d}^3\boldsymbol{v} f(\boldsymbol{x}, \boldsymbol{v})$. If the system is in equilibrium, we may also assume that it is in a steady state such that $\frac{\partial f}{\partial t} = 0$.

However, equations (1) and (2) are difficult to solve in practice. The distribution function is six dimensional, requiring full phase-space information. Worse still, we require its derivatives which amplify any noise in the data (even a million stars will sample only 10 points per phase-space dimension). As a result, there have been two types of methods proposed in the literature: take velocity moments of the Vlasov equation and solve the resulting Jeans equations (e.g. Bahcall 1984a,b,c); or guess the form of the distribution function and ask if the data are consistent with this (Kuijken & Gilmore 1989a,b,c). The first method has the advantage that we need not specify f, since we constrain it only through its moments. However, it throws away information about the shape of f. The latter method maximizes the available information but comes at the price of potentially fatal systematic errors if an incorrect form for f is assumed. Some mixed methods have also been proposed where the Jeans–Poisson system is solved, but the tracer density is closed by an integral over the measured (planar) distribution function (Fuchs & Wielen 1993; Flynn & Fuchs 1994).

In this paper, we focus on the moment-based methods that solve the Jeans–Poisson system of equations. This is because we want to make as few assumptions as possible to combat systematic errors. We do, however, also test the mixed method proposed by Fuchs & Wielen (1993) and applied to *Hipparcos* data by Creze et al. (1998) and Holmberg & Flynn (2000). This allows us to evaluate systematic errors introduced by assumptions about the form of f.

In the following sections, we review methods for recovering $\rho_{\rm s}$ (the in-plane disc matter density) and $\rho_{\rm dm}$ from the simultaneous solution of the Jeans and Poisson equations. We present first a new method based on minimal assumptions – our Minimal Assumption (MA) method. We then derive the method used in Holmberg & Flynn (2000) as a special case – the 'HF' method. We test both the MA and HF methods on our MW-like simulation in Section 3.

2.1 The MA method

The Jeans equations in cylindrical coordinates follow from velocity moments of the steady-state Vlasov equation (equation 1; Binney & Tremaine 2008). Consider first just the z Jeans equation:

$$\frac{1}{R}\frac{\partial}{\partial R}\left(R\nu_i \overline{v_{R,i} v_{z,i}}\right) + \frac{\partial}{\partial z}\left(\nu_i \overline{v_{z,i}^2}\right) + \nu_i \frac{\partial \Phi}{\partial z} = 0, \tag{3}$$

where ν_i, and $\overline{v_{z,i}^2}$ and $\overline{v_{R,i} v_{z,i}}$ are the density and velocity dispersion components, respectively, of a *tracer* population i moving in potential Φ.

We now introduce our only assumptions:

(i) The system is in equilibrium (steady-state assumption).

(ii) The dark matter density is constant over the range of $|z|$ considered.

(iii) The 'tilt' term: $\frac{1}{R}\frac{\partial}{\partial R}\left(R\nu_i \overline{v_{R,i} v_{z,i}}\right)$ is negligible compared to all other terms.

The first assumption is necessary for any mass-modelling method (e.g. Sánchez-Salcedo, Flynn & Hidalgo-Gámez 2011). The second assumption requires that the disc scaleheight is much smaller than the dark matter halo scalelength, $z_{\rm d} \ll r_{\rm h}$, or for disc-like dark matter, that the scaleheight of the dark disc is significantly larger than $z_{\rm d}$.

Binney & Tremaine (2008) show that the 'tilt' term is likely smaller than $(\overline{v_R^2} - \overline{v_z^2})(z/R)$ (see their discussion of the asymmetric drift in sections 4.8.2a and 4.9.3); so, assuming that $\overline{v_R^2}$ and $\overline{v_z^2}$ both decline with R as $\exp(-R/R_0)$ (applying also for our simulation, at least in the early stage, by construction), the *tilt term* in equation (3) is constrained by

$$\left|\frac{1}{R}\frac{\partial(R\nu\overline{v_R v_z})}{\partial R}\right| \simeq \frac{2\nu}{R_0}\overline{v_R v_z} \lesssim \frac{2\nu z}{R_0}\frac{\overline{v_R^2} - \overline{v_z^2}}{{\rm R}_\odot}. \tag{4}$$

The second term in equation (3) is of the order of $\nu\overline{v_z^2}/z_0$, where $z_0 \ll {\rm R}_\odot$, and $z_0 \ll R_0$ is the disc scaleheight. Hence, the neglected term is smaller than the second term by at least a factor of $2zz_0/(R_0{\rm R}_\odot)$. For these reasons, we define these assumptions as a 'minimal' set.

With the above assumptions, equation (3) becomes a function only of z and we can neglect the other two Jeans equations in R and θ. Our remaining Jeans equation becomes

$$\overline{v_{z,i}^2}\frac{\partial \nu_i}{\partial z} + \nu_i\left(\frac{\partial \Phi}{\partial z} + \frac{\partial \overline{v_{z,i}^2}}{\partial z}\right) = 0. \tag{5}$$

This is the Jeans equation for a one-dimensional slab. In principle, we should solve it for $R =$ constant. However, in practice, we must average over some range ΔR. We examine what is the maximum tolerable value of ΔR in Section 3.3.1.1.

For a given tracer population i, we can now write

$$\frac{{\rm d}\nu_i}{\nu_i} = -\frac{1}{\overline{v_{z,i}^2}}{\rm d}(\overline{v_{z,i}^2} + \Phi), \tag{6}$$

which can be solved straightforwardly:

$$\log\left(\frac{\nu_i}{\nu_i(0)}\right) = -\log\left(\frac{\overline{v_{z,i}^2}}{\overline{v_{z,i}^2}(0)}\right) - \int_0^z \frac{1}{\overline{v_{z,i}^2}}\frac{{\rm d}\Phi}{{\rm d}z}\,{\rm d}z. \tag{7}$$

Thus, at each height above the disc, z_*, the density of the tracer population, $\nu_i(z_*)$, can be calculated as

$$\frac{\nu_i(z_*)}{\nu_i(0)} = \frac{\overline{v_{z,i}^2}(0)}{\overline{v_{z,i}^2}(z_*)}\exp\left(-\int_0^{z_*}\frac{1}{\overline{v_{z,i}^2}(z)}\frac{{\rm d}\Phi}{{\rm d}z}\,{\rm d}z\right). \tag{8}$$

This general equation for $\nu_i(z)$ can be used to describe all the visible components of the disc. Given the density at the mid-plane, $\nu_i(0)$, and the vertical velocity dispersion, $\overline{v_{z,i}^2}(z)$, as a function of z, for each of the gas and stellar populations in the local disc, we can model the full disc density distribution as

$$\rho_{\rm s}(z) = \sum_i m_i^* \nu_i(0)\frac{\overline{v_{z,i}^2}(0)}{\overline{v_{z,i}^2}(z)}\exp\left(-\int_0^z \frac{1}{\overline{v_{z,i}^2}}\frac{{\rm d}\Phi}{{\rm d}z}\,{\rm d}z\right), \tag{9}$$

where m_i^* is the mass-to-light ratio for a given population i. The Poisson equation then determines the potential Φ from the density. In cylindrical polar coordinates, this is given by

$$4\pi G\rho = \frac{\partial^2\Phi}{\partial z^2} + \frac{1}{R}\frac{\partial}{\partial R}\left(R\frac{\partial\Phi}{\partial R}\right) = \frac{\partial^2\Phi}{\partial z^2} + \frac{1}{R}\frac{\partial V_c^2(R)}{\partial R}, \quad (10)$$

where ρ is now the *total mass density* and $V_c(R)$ is the circular velocity at radius R.

Splitting the matter density ρ into disc contributions (gas+stars) that vary with z, $\rho_s(z)$[4], and an effective dark matter contribution that includes the circular velocity term (ρ_{dm}^{eff}), the Poisson equation becomes

$$\frac{\partial^2\Phi}{\partial z^2} = 4\pi G[\rho_s(z) + \rho_{dm}^{eff}] \quad (11)$$

with

$$\rho_{dm}^{eff} = \rho_{dm}(R) - (4\pi GR)^{-1}\frac{\partial}{\partial R}V_c^2(R), \quad (12)$$

where $\rho_{dm}(R)$ is the halo mass density [following assumption (ii), this is assumed to be independent of z in the volume considered) and $V_c(R)$ is the (total) circular velocity at a distance R (in the plane) from the centre of the Galaxy. For a flat rotation curve, the second term vanishes and $\rho_{dm}^{eff}(R) = \rho_{dm}(R)$. Note that there is an important difference between the vertical velocity dispersion of a tracer population, $\overline{v_{z,i}^2}(z)$, in equation (8), and the same quantity as it appears in the mass model (equation 9). The former is something that we must measure for our chosen tracers, while the latter is simply a parameter that appears in our disc mass model. The two only become equivalent in the limit that we have data for every single disc star. To put it another way, the tracers *must* satisfy equation (8), but we could replace equation (9) with some other mass model for the disc.

We may now solve equations (9) and (2) numerically for a given tracer population. We adopt the following procedure: first, we make initial trial guesses for $\rho_s(0)$ (and any other unknowns in the star/gas disc), ρ_{dm}, and the run of vertical velocity dispersion for the tracers $\overline{v_{z,i}^2}(z)$. Next, we solve equation (9) to obtain $\Phi(z)$ and its first derivative $\frac{\partial\Phi}{\partial z}$, with $\Phi(0) = \left.\frac{\partial\Phi}{\partial z}\right|_0 = 0$. Then, we plug this result into equation (8) to obtain the vertical density fall-off of the tracers, $\nu_i(z)$. Finally, this is compared with the observed distribution to obtain a goodness-of-fit. In principle, each tracer population gives us an independent constraint on $\Phi(z)$. A useful consistency check then follows since all tracers should yield the same potential, while combining different tracers gives smaller errors on the derived parameters. Note that the above procedure requires many input parameters that are typically poorly constrained, for example, the normalizations and dispersions of each of the disc components and the vertical dispersion profile of the tracers. To efficiently explore this parameter space and marginalize over the uncertainties, we use an MCMC method. This is described in Section 2.3.

Our MA method requires a measurement of $\overline{v_{z,i}^2}(z)$ for each tracer population considered. The HF method we derive next does not require $\overline{v_{z,i}^2}(z)$ – using an additional assumption of separability instead. This has several advantages, but comes with a risk that this additional assumption will lead to systematic bias. We examine this in detail in Section 3.

2.2 The Holmberg & Flynn method

The HF method (Fuchs & Wielen 1993; Holmberg & Flynn 2000) adds four additional assumptions:

(i) The potential is separable: $\Phi(R, z) = \Phi(R) + \Phi(z)$.

(ii) The distribution function of tracers also separates. At a fixed cylindrical radius in the disc, it is a function only of the vertical energy: $f = f(E_z)$.

(iii) All disc components are isothermal.

(iv) The rotation curve contribution to the Poisson equation – $(4\pi GR)^{-1}\frac{\partial}{\partial R}V_c^2(R)$ – is negligible. Thus, $\rho_{dm} = \rho_{dm}^{eff}$ by construction.

The first two assumptions are critical for the method and also lie at the heart of the method proposed by Kuijken & Gilmore (1989c). Thus, testing their validity applies to a wider range of past methods. Note that if these two assumptions are satisfied, then the 'tilt' term in the Jeans equation is exactly zero, thus perfectly satisfying assumption (iii) of the MA method. However, the MA method makes the weaker assumption that the tilt term is *small* as compared to the other terms in the Jeans equations. Unlike the HF method, it requires no assumptions about the form of the potential or the distribution function. It is the latter that is the key difference between the two. If the motion is not separable, then the distribution function cannot be approximated by $f = f(E_z)$. As we will demonstrate in Section 3, this assumption leads to significant systematic errors even at $\sim$1.5 disc scaleheights above the plane. By contrast, assuming that the tilt term is simply small appears to be robust even up to several disc scaleheights.[5]

The HF method is a mixed method that uses the Jeans equations (as in the MA method), but assumes that each disc component is isothermal. This gives a Jeans equation as a function of z similar to that in the MA method:

$$\overline{v_{z,i}^2}\frac{\partial\nu_i}{\partial z} + \nu_i\frac{\partial\Phi(z)}{\partial z} = 0 \quad (13)$$

which is independent of R and can then be straightforwardly solved to give

$$\nu_i = \nu_{0,i}\exp\left(-\frac{\Phi(z)}{\overline{v_{z,i}^2}}\right), \quad (14)$$

where $\nu_{0,i} = \nu_i(0)$.

Thus, the density of the disc, ρ_s, can be written as a sum over isothermal components:

$$\rho_s(z) = \sum_i m_i^*\nu_{i,0}\exp\left(-\frac{\Phi(z)}{\overline{v_{z,i}^2}}\right), \quad (15)$$

where m_i^* is the mass-to-light ratio for a given population i. With the above decomposition, non-isothermality can still be modelled as a linear combination of a larger number of isothermal distributions (Bahcall 1984a). However, this expansion is degenerate and

[4] Note that, throughout, we use the notation $\rho_s = \rho_s(0)$ – the in-plane baryonic mass density.

[5] Note that should the tilt term become large, then, in principle, we could correct for it in the Jeans equation. This is perfectly possible in the MA method, but problematic for the HF method. In the HF method, we would also have to correct for it in the distribution function. Such tilt corrections are, however, beyond the scope of this paper.

introduces many additional parameters that become expensive to explore (Kuijken & Gilmore 1989c).

Plugging equation (15) into Poisson equation (11), we can then calculate the gravitational potential, assuming a constant contribution for the dark matter density.

As in our MA method, the HF equations are closed by comparing the observed fall-off of the tracer population with the predicted one (given an initial guess of the disc model and dark matter density parameters). However, instead of using the solution to the moment equation (8) (or equation 14), they calculate the density fall-off of the tracers from the integral of the distribution function (Fuchs & Wielen 1993; Flynn & Fuchs 1994). Here they use the additional assumptions (reasonably close to the mid-plane) that the potential is separable, $\Phi(R, z) = \Phi(R) + \Phi(z)$, and that the distribution function of tracers is a function only of the vertical energy: $f = f(E_z)$. This has two key advantages. First, it maximizes the use of information in the data since it uses the *shape* of the distribution function, rather than just its lowest moments as in the MA method above. Secondly, one needs only measure f at one height z above the disc – $\overline{v_{z,i}^2}(z)$ is not required. We may understand this as follows. The density of the tracers is given by

$$\nu_i(z) = \int_{-\infty}^{\infty} \mathrm{d}v_z f(E_z) = 2\int_0^{\infty} \mathrm{d}v_z \left[f\left(\frac{1}{2}v_z^2 + \Phi\right)\right], \qquad (16)$$

and, since $f = f(E_z)$, we can rewrite equation (16) as an Abel integral:

$$\nu_i(z) = 2\int_{\Phi(z)}^{\infty} \mathrm{d}(\sqrt{2E_z})\sqrt{2E_z}\frac{f(\sqrt{2E_z})}{\sqrt{2\,(E_z - \Phi)}}. \qquad (17)$$

Then, substituting $|w_0| = \sqrt{2E_z}$ and using $f(\sqrt{2E_z}) = f(w_0)$, we obtain

$$\nu_i(z) = 2\int_{\sqrt{2\Phi}}^{\infty} \frac{f(w_0)w_0 dw_0}{\sqrt{w_0^2 - 2\Phi}}, \qquad (18)$$

where w_0 is the vertical velocity of stars in the mid-plane ($z = 0$). Thus, we can measure $f(E_z)$ – valid for all heights about the disc z – from $f(|w_0|)$ measured only in the disc plane.

Note that the above does not assume that the tracers are isothermal, though the mass model (equation 15) does. This will become inconsistent if the tracers comprise most of the mass of the disc. In practice, this is unlikely to be the case. However, the inconsistency can always be avoided by using the more general mass model derived in the MA method, while still closing the equations using equation (18). We test the effect of this inconsistency in Section 3.

We stress that the assumption of $f = f(E_z)$ is likely to be valid close to the disc plane. Thus, the HF method as employed in Holmberg & Flynn (2000) – where they probe only up to ∼1 half-mass scaleheight above the disc – is unlikely to be biased. However, as we probe to heights greater than the disc scaleheight, systematics will creep in. Furthermore, probing to such heights – as we shall show – is necessary for breaking a degeneracy between $\rho_{\rm dm}$ and $\rho_{\rm s}$. We explore the effect of the $f = f(E_z)$ assumption in Section 3.

2.3 Determining $\rho_{\rm dm}$ and $\rho_{\rm s}$ with an MCMC

In summary, while the MA and HF methods differ in their underlying assumptions, the basic strategy for recovering the local matter density is the same:

(i) Build a mass model for the local mass distribution consisting of components ν_i, defined by equation (8) (or equation 14), for gas and stellar populations and a constant contribution for dark matter $\rho_{\rm dm}$.

(ii) Use this mass model to integrate the Poisson equation (11) and the Jeans equation (5) (or equation 13) simultaneously to compute the local potential Φ (and its z-derivative).

(iii) Use the calculated potential Φ and the measured kinematics of the tracers to compute their density fall-off, $\nu(z)$ (using equation 8 or 18). To predict the density fall-off of the tracers, the HF method needs the measure of their vertical velocity distribution function in the mid-plane, $f(w_0)$, while in the case of the MA method, the vertical velocity dispersion as a function of z – $\overline{v_{z,i}^2}(z)$ – is required.

(iv) Compare the predicted density profile(s), $\nu(z)$, with the observed one(s), $\nu_{\rm obs}(z)$, to reject or accept the model input parameters: $\rho_{\rm dm}$ and parameters governing each of the components ν_i.

In practical applications, the above implies many (degenerate) free parameters if the disc model has many non-isothermal components with parameters that are poorly known, while $\overline{v_{z,i}^2}(z)$ for the tracers may also be poorly constrained. An MCMC provides an efficient way to rapidly explore this parameter space. It naturally deals with parameter degeneracies: all of the unknown parameters are 'marginalized out' to leave the key parameters of interest in (the total matter density, $\rho_{\rm tot}$, and the dark matter density, $\rho_{\rm dm}$). In this way, the MCMC addresses some of the issues raised by Kuijken & Gilmore (1989a,b,c) about degeneracies between parameters in very complex models, making such models unworkable.

We use an MCMC method based on a Metropolis algorithm (e.g. Saha 2003) to recover the local density. For the simulation data, we use the dark matter density (namely $\rho_{\rm dm}$ in equation (12), adding the rotation curve term calculated for each volume) and the visible matter density $\rho_{\rm s}$ (which corresponds to $\nu_{i,0} = m_i^* \nu_i(0)$ in equation 9 or 15), as our input parameters. When we apply the HF method, we fit the distribution function at the mid-plane with a Gaussian (double Gaussian) for the unevolved (evolved) simulation. These fits are good for most of the volumes considered (an example is shown in the left-hand panel of Fig. 2). When we adopt the MA method, we linearly interpolate the velocity dispersion of the tracers above the plane, $\overline{v_{z,i}^2}(z)$, since this method is extremely sensitive to the velocity dispersion function adopted.

When we apply the two methods to the real data (see Section 4), the situation is more complex. First, we must fit a larger number of parameters, namely the local dark matter density $\rho_{\rm dm}$, the total visible density $\rho_{\rm s}$, the fraction of the different disc components $\nu_{i,0}$ and their velocity dispersions in (and even potentially above) the plane $\overline{v_{z,i}^2}$. Secondly, the data are magnitude rather than volume limited. We take this into account by drawing the observed stellar distribution from the model density fall-off using the observed luminosity function. The MCMC allows us to easily implement both these additional parameters and the sampling of the luminosity function. In addition, it is straightforward to model different tracer populations simultaneously and apply constraints on the local *surface density* of the disc. Our full procedure is described in more detail in Section 4. Finally, with real data, we cannot simply interpolate the velocity dispersion as a function of z, but we must consider the uncertainties on the velocities. Such uncertainties can be straightforwardly added to the MCMC and marginalized out (see Appendix C).

We apply the MA and HF methods to our simulated MWs in Section 3. We then apply the MA method to real data in Section 4. For the simulation, we calculate the potential by modelling the visible matter in the disc as a single population. To simplify the calculation, we introduce some dimensionless parameters described in Appendix A (Bahcall 1984a,b,c). This transforms equations (8), (14) and (11) to equations (A8), (A11) and (A9), respectively.

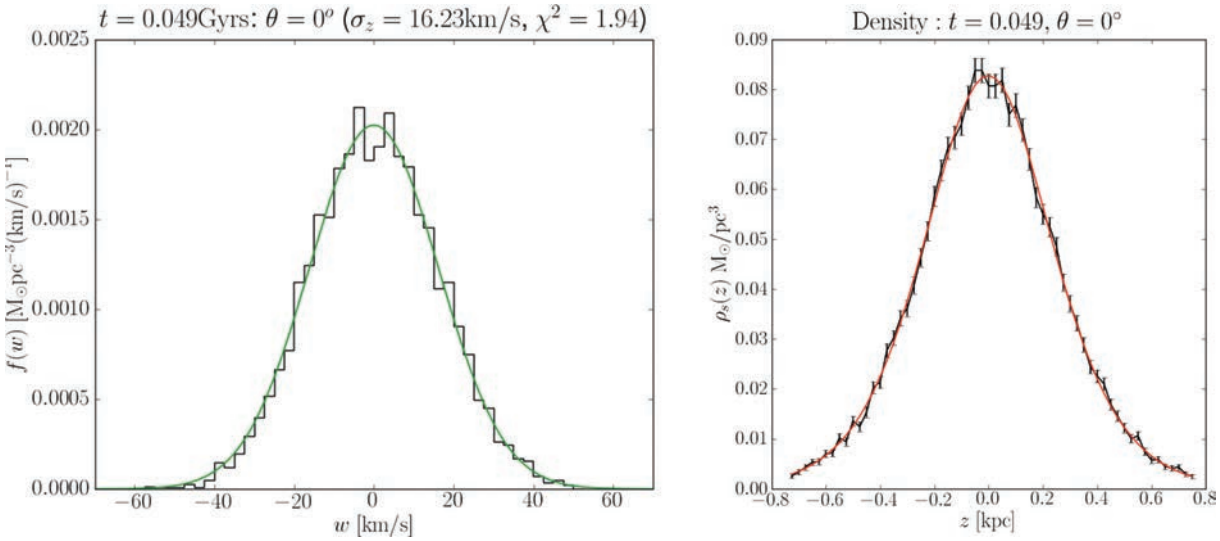

Figure 2. Left-hand panel: the vertical velocity distribution of star particles (in black) for one of the 'wedge' patches at $R_\odot = 8.5$ kpc from the centre of the galaxy. The green curve corresponds to the Gaussian fit. Right-hand panel: the vertical density distribution of star particles (in black) for one of the 'wedge' patches at $R_\odot = 8.5$ kpc from the centre of the galaxy. The red curve corresponds to the prediction of the best-fitting mass model. The error bars represent Poisson noise.

3 TESTING THE METHODS

To test the MA and HF methods discussed in Section 2 and evaluate the systematic errors, we apply both to a high-resolution collisionless simulation of a MW-like galaxy.

We consider two different stages of the simulation: an unevolved one with an axisymmetric disc (shown in the left-hand panel of Fig. 3) and fulfilling all the hypotheses of the more restrictive HF method; and a more evolved stage (represented in Fig. 3, right-hand panel) presenting a bar, similar to the real MW, that breaks many of the assumptions. The results for these two different stages of the simulation are described in Sections 3.3.1 and 3.3.2, respectively.

3.1 The simulation

We ran a simulation of a MW-like galaxy with the parallel tree code PKDGRAV (Stadel 2001), using the galaxy models of Widrow & Dubinski (2005) for the initial conditions. These models are derived from a composite three-integral distribution function

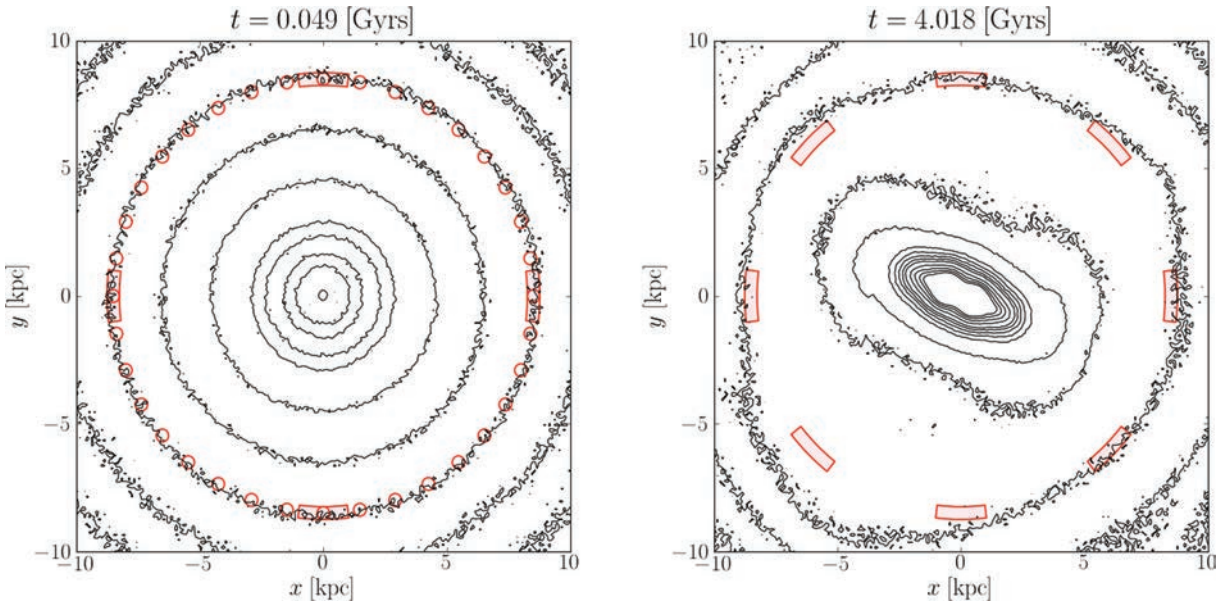

Figure 3. Density contours viewed from top for the disc star particles. Left-hand panel: an early time-step ($t \sim 0.05$ Gyr) presenting an axisymmetric disc. Right-hand panel: the evolved simulation ($t \sim 4$ Gyr), presenting a bar and spiral arms with interarm contrast $\rho_{arm}/\rho_{dip} \simeq 0.15$. The red circles correspond to the position of the cylindrical 'solar neighbourhood' patches, at a distance of $R_\odot = 8.5$ kpc from the Galactic Centre. The red-shaded wedges represent the other volumes we used to compare the results of the analysis of the two stages of the simulation. We adopt patches of this shape to obtain better sampling. The angular position of the patches is calculated from $x, y = [R_\odot, 0]$ anticlockwise.

$f = f_{\rm disc}(E, E_z, L_z) + f_{\rm halo}(E) + f_{\rm bulge}(E)$ and provide near-equilibrium initial conditions.

The disc model has an exponential radial profile and a $\mathrm{sech}^2(z/z_s)$ vertical profile. Its distribution function applies in the epicyclic approximation with $\sigma_{R,\phi,z} \ll V_c$, so the vertical energy is an approximate integral of motion: this leads to triaxial velocity ellipsoids in the disc models as seen in real spiral galaxies (Widrow, Pym & Dubinski 2008). The halo is modelled as a Navarro–Frenk–White profile. However, when its distribution function is combined with the disc one, the net halo density profile is slightly flattened along the z-axis near the centre, but preserving the r^{-1} central cusp.

To have statistics comparable with the present data in the solar neighbourhood [e.g. Holmberg & Flynn (2000) considered ∼2000 A stars in a cylindrical volume of radius $R = 200$ pc and height $|z| < 200$ pc centred on the Sun], we constructed a disc with $n_d = 30 \times 10^6$ star particles. We chose the masses of the dark matter halo particles and the (star) bulge particles so that the heating time-scale for the disc is much larger than both the internal relaxation time-scale and the time of the simulation (∼4 Gyr): $t_{\rm heat} \gg t_{\rm rel} \gg t_{\rm sim}$, where $t_{\rm rel}$ is given by (Binney & Tremaine 2008):

$$t_{\rm rel} = n_{\rm rel} t_{\rm cross} = \frac{n}{8 \log \Lambda} \frac{b_{\rm max}}{v_{\rm typ}}, \quad (19)$$

where $v_{\rm typ} = \sqrt{GM/\mathrm{R}_\odot}$ is the typical velocity at the solar position, $\mathrm{R}_\odot = 8.5$ kpc, $b_{\rm min} = 2Gm_{\rm part}/v_{\rm typ}^2$, $b_{\rm max} = \mathrm{R}_\odot$ and the Coulomb logarithm is $\log \Lambda = \log(b_{\rm max}/b_{\rm min})$. Given $n_d = 30 \times 10^6$ total stars, the number enclosed within $\mathrm{R}_\odot$ is $n = n_d(\mathrm{R}_\odot) \sim 25 \times 10^6$. Using the latter number, we find $t_{\rm rel} \simeq 1.17 \times 10^4$ Gyr.

The heating time $t_{\rm heat}$ is given by (Lacey & Ostriker 1985)

$$t_{\rm heat} = \frac{\sigma_z^2 V_h}{8\pi G^2 M_h \rho_h \log \Lambda_h}, \quad (20)$$

where σ_z is the vertical velocity dispersion of the disc particles, M_h is the mass of the dark matter particles, V_h is their typical velocity, and ρ_h and $\log \Lambda_h$ are the density and the Coulomb logarithm for the halo (a similar calculation can be done for the bulge particles).

Using $t_{\rm heat} = k t_{\rm rel}$, with $k \sim 10$, we find the following satisfy the above time-scale constraints: $n_h = 15 \times 10^6$ and $n_b = 0.5 \times 10^6$ particles for the halo and bulge, respectively.

The main features of the model we used are listed in Table 1. For comparison, some of the corresponding features of the real MW are given in Table 2.

In our analysis, we consider two different outputs of the simulation: an unevolved stage ($t \sim 50$ Myr) in which the disc is still axisymmetric and an evolved one ($t \sim 4$ Gyr) which presents a bar similar to the real MW. These two stages are shown in Fig. 3 (left-hand and right-hand panels, respectively). The unevolved disc is used to test the method in general and to study what data are needed to recover the right value of the local density in the ideal case of data fulfilling all the assumptions. The evolved stage represents a more realistic situation and is used to test the effect of realistic disc inhomogeneities on the determination of the local density. The spiral arms – that are the major driver of inhomogeneities at the solar neighbourhood in the evolved disc – are compatible with the MW: our Galaxy has an interarm ratio of the spiral structure at the solar radius $\mathrm{R}_\odot$ of $K \sim 1.7$ (Drimmel & Spergel 2001); the corresponding value for the simulation is $K \sim 1.5$.

Table 1. Parameters for the disc, dark matter halo and stellar bulge for the initial conditions of the simulation. From the left-hand to right-hand side, the columns show the number of particles (N); the total mass (M); the softening length (ε); the half-mass scalelength ($R_{1/2}$); and the half-mass scaleheight ($z_{1/2}$).

	N (10^6)	M ($10^{10}\,\mathrm{M}_\odot$)	ε (kpc)	$R_{1/2}$ (kpc)	$z_{1/2}$ (kpc)
Disc	30	5.30	0.015	4.99	0.17
Bulge	0.5	0.83	0.012	–	–
Halo	15	45.40	0.045	–	–

Table 2. The distinct components of the MW. From the left-hand to right-hand side, the columns show the total mass (M); the half-mass scalelength ($R_{1/2}$); and the half-mass scaleheight ($z_{1/2}$). These values are compiled using the following relations: $z_{1/2} = 0.55 z_s = 0.7 z_0$ and $R_{1/2} = 1.68 R_0$ (Read et al. 2008), where z_s is the sech^2 disc scaleheight, z_0 is the exponential disc scaleheight and R_0 is the exponential disc scalelength.

	M ($10^{10}\,\mathrm{M}_\odot$)	$R_{1/2}$ (kpc)	$z_{1/2}$ (kpc)	Reference
Thin disc	3.5–5.5[a]	3.35–9.24	∼0.14–0.18	fl, o, fe, k
Thick disc	–	5.04–7.56	0.49–0.84	o, n, s
Bulge	∼1	–	–	d, fl
Halo	∼40–200	–	–	x, g

[a]Total disc mass.

References: fl = Flynn et al. (2006); o = Ojha (2001); fe = Feast (2000); k = Kuijken & Gilmore (1989b); n = Ng et al. (1997); s = Spagna et al. (1996); d = Dehnen & Binney (1998); x = Xue et al. (2008); and g = Guo et al. (2010).

In the analysis of the simulation, we set the solar neighbourhood position at a Galactocentric distance of $\mathrm{R}_\odot = 8.5$ kpc, in agreement with the International Astronomy Union recommended value. We consider several small volumes at different angular positions around the disc, represented by the red circles and wedges in Fig. 3 (also see Section 3.3). For the unevolved (axisymmetric) disc, these different patches test the effect of sampling error on our derived $\rho_{\rm dm}$ and ρ_s; for the evolved disc, they examine the effect of disc inhomogeneities.

3.2 How well does the simulation satisfy our assumptions?

Both the MA and HF methods are based on several key assumptions, as outlined in Sections 2.1 and 2.2. To understand how well both methods can recover the local dark matter density, we first evaluate how well the two stages of the simulation fulfil these assumptions.

3.2.1 Constant ρ_{dm} in the local volume

Hypothesis (ii) of the MA method is well fulfilled as shown in Fig. 4, where we plot the dark matter density as a function of z for the unevolved (left-hand panel) and the evolved (right-hand panel) simulations. The purple line represents $|z| = 0.75$ kpc, that is, the maximum height considered in our analysis.

3.2.2 Isothermality, tilt and equilibrium

The velocity dispersion $\overline{v_z^2}$ as a function of z should be constant, by definition, for an isothermal population. Inthe two left-hand panels of Fig. 5, the velocity dispersion $\overline{v_z^2}(z)$ is represented for the two output times of the simulation considered ($t = 0.049$ Gyr in the upper panel and $t = 4.018$ Gyr in the lower one) at $R = 8.5$ kpc (in red). For comparison, the observational data for the MW (blue data points), and the best-fitting $\overline{v_z^2}(z)$ function determined by Bond et al. (2010) (green dashed line: the light green shaded region represents the errors in the fit parameter), are shown. Bond et al.'s (2101) fit

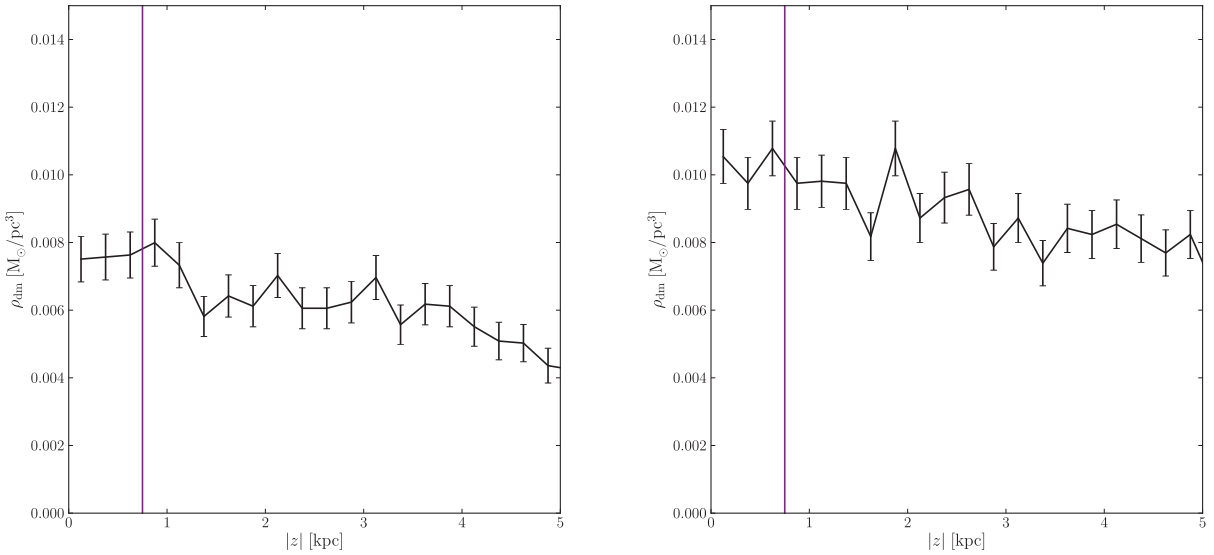

Figure 4. The dark matter density as a function of $|z|$ for the the unevolved (left-hand panel) and evolved (right-hand panel) simulations. The purple line represents $z = 0.75$ kpc, that is, the maximum height considered in our analysis. The error bars correspond to the Poisson errors. The dark matter density is noisy owing to the large mass of the dark matter particles, but it is constant within the uncertainties for $|z| < 0.75$ kpc.

is obtained from a sample of 53 000 blue ($0.2 < g - r < 0.6$) disc stars from the SDSS with radial velocity measurements, $b > 20^\circ$ and high metallicity ([Fe/H] > -0.9), up to $|z| < 5$ kpc. These stars are taken at high z over the plane and are much hotter than the stars used in the literature (A, F and K stars) to trace the local gravitational potential (blue dots). However, the fit does give us information about the potential non-isothermality of the disc. The dashed yellow line is the isothermal line for 8.5 kpc. These plots refer to a particular angular position in the disc ($\theta = 0^\circ$), but the situation for $\overline{v_z^2}$ is similar for the whole disc.

The visible population in the disc for the unevolved stage ($t = 0.049$ Gyr) of the simulation is almost perfectly isothermal, while a significant deviation from isothermality is seen for the more evolved stage ($t = 4.018$ Gyr).

When the disc species are not isothermal, the second term of the Jeans equation (3) cannot be approximated as $\overline{v_{z,i}^2}\partial\nu_i/\partial z$, but we must consider also the contribution of the z-derivative of $\overline{v_{z,i}^2}(z)$.

To quantify the effect of non-isothermality, we look at the the second and third terms of the Jeans equation (3) calculated for the two stages of our simulation. We compute these terms using a smoothed particle hydrodynamics (SPH) like method to determine smoothed quantities and gradients at the particle positions (for more details see Appendix B).

In Fig. 6, the SPH-calculated quantities are plotted for the two stages of the simulation considered, $t = 0.049$ Gyr (left-hand panel) and $t = 4.018$ Gyr (right-hand panel) for $\theta = 0^\circ$. The red line represents the potential term. The solid black and the dashed grey lines represent the sum of the last two terms of the Jeans equation in the non-isothermal ($r_{\rm NI}$) and isothermal ($r_{\rm I}$) cases, respectively, namely

$$r_{\rm NI} = \nu_i \frac{\partial\Phi}{\partial z} + \frac{\partial(\overline{v_{z,i}^2}\nu_i)}{\partial z} \quad \text{(non-isothermal)} \tag{21}$$

and

$$r_{\rm I} = \nu_i \frac{\partial\Phi}{\partial z} + \overline{v_{z,i}^2}\frac{\partial\nu_i}{\partial z} \quad \text{(isothermal)}. \tag{22}$$

We see in this figure that, for $t = 0.049$ Gyr, the second terms calculated as isothermal ($\overline{v_{z,i}^2}\partial\nu_i/\partial z$, dashed cyan line) and including non-isothermality [$\partial(\nu_i\overline{v_{z,i}^2})/\partial z$, solid blue line] overlap almost perfectly, and that $r_{\rm NI}$ (black continuous line) and $r_{\rm I}$ (grey dashed line) are also very similar and close to zero. This is not surprising since the velocity dispersion $\overline{v_{z,i}^2}$ is almost constant with z in the unevolved stage of the simulation.

As expected from Fig. 5, this is not the case for the simulation at $t = 4.018$ Gyr where the isothermal (cyan) and the non-isothermal (blue) second-term lines are clearly different. In this case, $r_{\rm I}$ and $r_{\rm NI}$ are distinct and, while the non-isothermal residual averages to zero, the isothermal one presents a positive (negative) feature for $z < 0$ ($z > 0$). This suggests that using the isothermal approximation for the evolved stage of the simulation will introduce a bias that must be corrected. We show this in Section 3.3.1.

Finally, note that the sum of the second and third terms of the Jeans equation in Fig. 6 is consistent with zero, excluding the presence of an important *tilt term* [hypothesis (iii) of the MA method] or significant non-equilibrium effects [hypothesis (i)].

3.2.3 *A flat rotation curve*

The second term of equation (12) is zero for flat rotation curves, that is, for $V_{\rm c}(R) = (R{\rm d}\Phi/{\rm d}R)^{1/2} = $ constant. For a flat rotation curve, the effective dark matter density corresponds to the halo mass density, $\rho_{\rm dm}^{\rm eff} = \rho_{\rm dm}(R)$, while the effect of a rising (falling) rotation curve is to give rise to a term of opposite (similar) sign to $\rho_{\rm dm}$, causing an underestimation (overestimation) of the dark matter density in the disc.

In Fig. 7, the rotation curves for the unevolved stage of the simulation ($t = 0.049$ Gyr) and for the evolved one ($t = 4.018$ Gyr) are plotted in the left-hand and the right-hand panels, respectively. For the unevolved simulation, the rotation curve is almost flat or slightly falling, while for the more evolved stage, in general, the rotation curve is usually slightly rising for $R = 8.5$ kpc; this means that we would expect a systematic underestimation of $\rho_{\rm dm}$ at $R = 8.5$ kpc for the evolved simulation.

To quantify the effect on the determination of $\rho_{\rm dm}$, we compute $V_{\rm c}(R) = (R{\rm d}\Phi/{\rm d}R)^{1/2}$ in large R bins (1 kpc) along a 'slice' of the disc for each angular position considered using the SPH method,

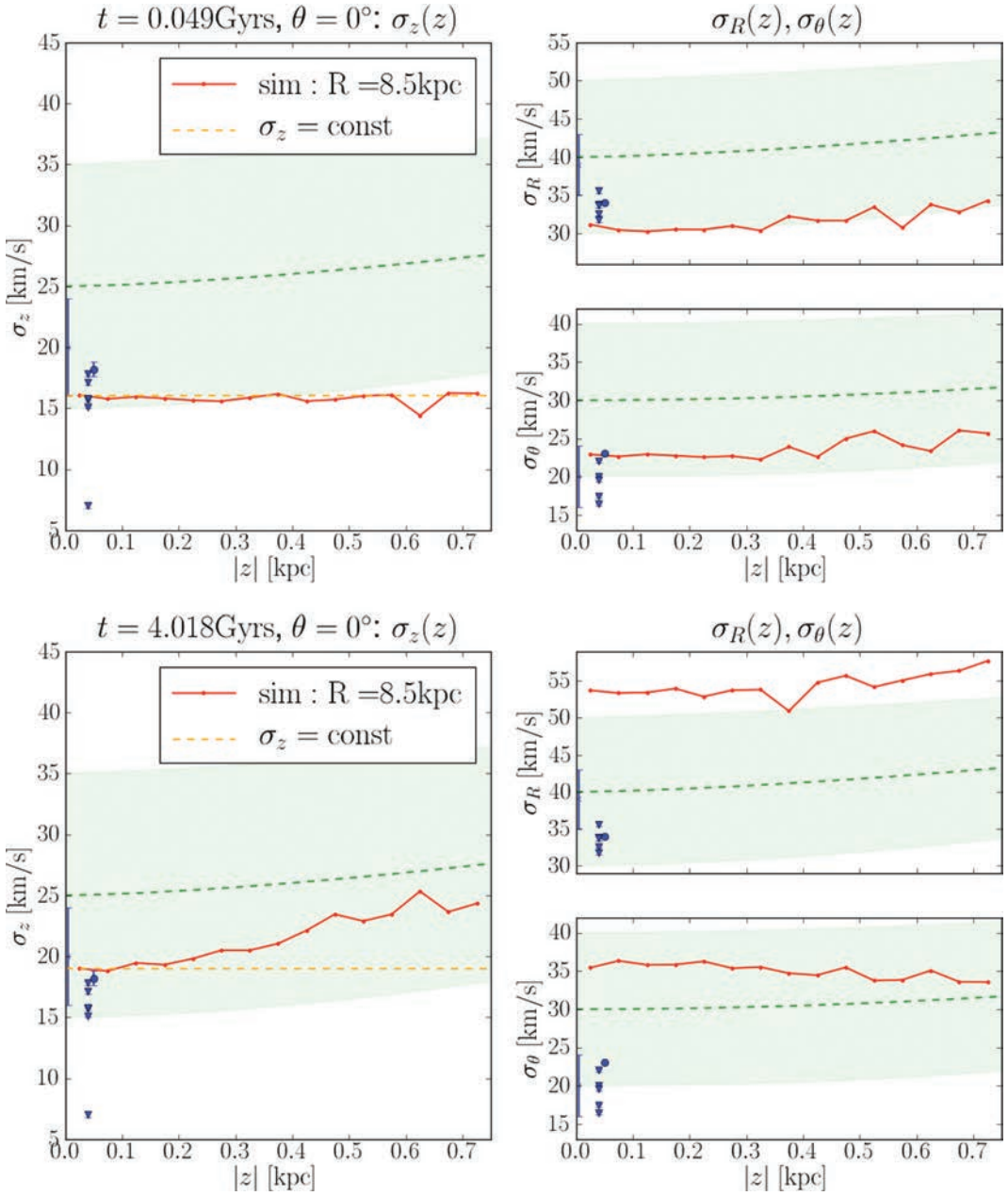

Figure 5. Velocity dispersion gradients with z. Upper panels: unevolved simulation ($t = 0.049$ Gyr). Lower panels: evolved simulation ($t = 4.018$ Gyr). The dashed green line represents the best fit of the velocity dispersion by Bond et al. (2010), while the green-shaded region shows the errors in the fitted parameters. The blue data points give the values of $\overline{v_z^2}(z)$, $\overline{v_\theta^2}(z)$ and $\overline{v_R^2}(z)$ taken from the literature (Holmberg & Flynn 2004; Seabroke & Gilmore 2007). The red points represent the values for our simulation at $R = 8.5$ kpc. The yellow and red dot–dashed lines in the $\overline{v_z^2}(z)$ plot are lines of constant $\overline{v_z^2}(z)$.

then we calculate its $\partial/\partial R$ derivative to estimate the second term of equation (12): $|(4\pi G R)^{-1}\partial V_c^2/\partial R|$. In Fig. 8, the absolute values of these terms are plotted for $\theta = 0^\circ$ at $t = 0.049$ Gyr (left-hand panel) and $t = 4.018$ Gyr (right-hand panel). The black crosses show the values of $\rho_{\rm dm}$ at $R = 8.5$ kpc. For the evolved simulation, the shape of these plots is slightly different for the various angular positions at small R, due to the presence of the bar. However, at $R = 8.5$ kpc, the contribution of the rotation curve term is between 10 and 30 per cent of $\rho_{\rm dm}$ (with positive sign). The shape of the rotation curve term with R is always similar around the disc for the unevolved simulation and its contribution is ∼15–20 per cent of $\rho_{\rm dm}$ at $R = 8.5$ kpc, always with negative sign.

For the real MW, we can estimate the contribution of the rotation curve term from the Oort constants (Binney & Merrifield 1998):

$$(4\pi G R)^{-1}\frac{\partial V_c^2}{\partial R} = \frac{B^2 - A^2}{2\pi G}. \quad (23)$$

To determine the Oort constants, we must use stellar tracers that are well-mixed. As for the vertical potential determination, this means avoiding young stars. The most recent estimates using F giants (Branham 2010) and K–M giants (Mignard 2000) from *Hipparcos* give $A = 14.85 \pm 7.47\,{\rm km\,s^{-1}\,kpc^{-1}}$ and $B = -10.85 \pm 6.83\,{\rm km\,s^{-1}\,kpc^{-1}}$, and $A = 14.5 \pm 1.0\,{\rm km\,s^{-1}\,kpc^{-1}}$ and $B = -11.5 \pm 1.0\,{\rm km\,s^{-1}\,kpc^{-1}}$, respectively. This is ∼−35 per cent of

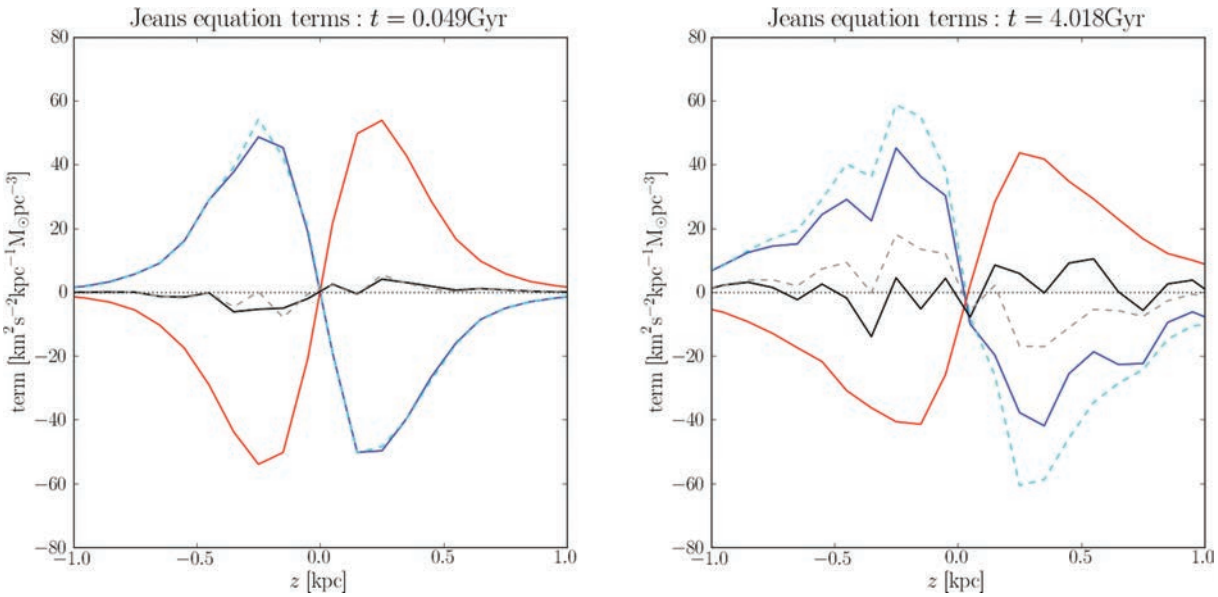

Figure 6. The second and third terms of the Jeans equation (3), calculated for our simulation at $t = 0.049$ Gyr (left-hand panel) and $t = 4.018$ Gyr (right-hand panel) for $\theta = 0^\circ$, with the SPH-like method. The different lines represent: dashed cyan: $\overline{v_{z,i}^2}\partial\nu_i/\partial z$ (second term: isothermal); solid blue: $\partial(\nu_i\overline{v_{z,i}^2})/\partial z$ (second term: non-isothermal); and solid red: $\nu_i\partial\Phi/\partial z$ (third term). The black and grey lines are the 'residuals' given by the sum of the terms: solid black: $\nu_i\partial\Phi/\partial z + \partial(\overline{v_{z,i}^2}\nu_i)/\partial z$ (non-isothermal); and dashed grey: $\nu_i\partial\Phi/\partial z + \overline{v_{z,i}^2}\partial\nu_i/\partial z$ (isothermal).

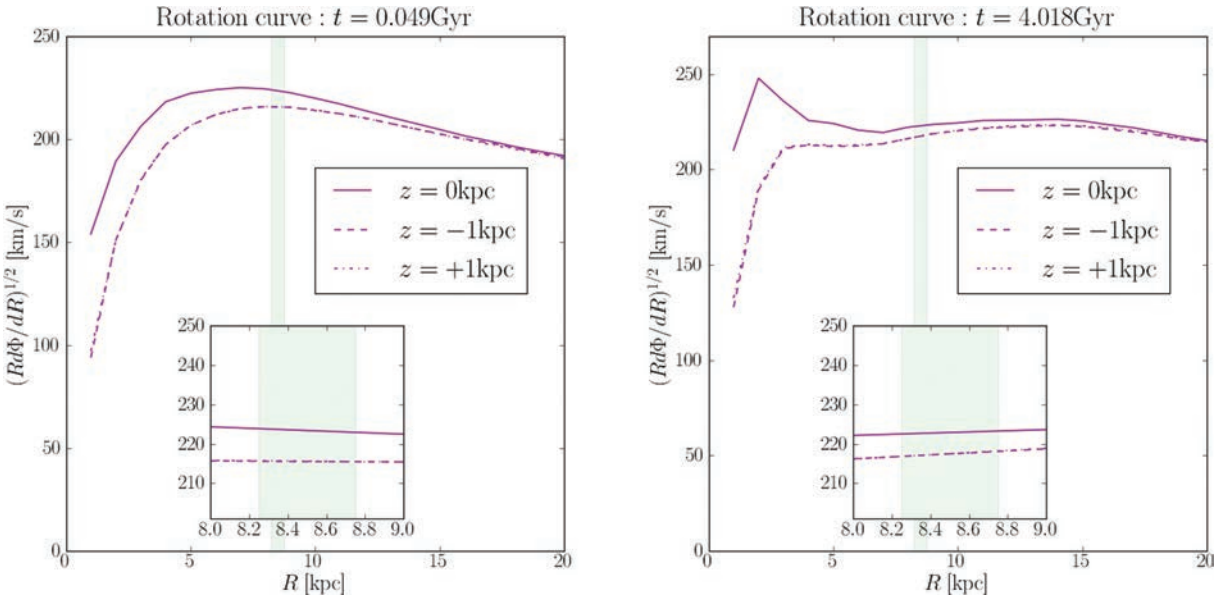

Figure 7. Rotation curve for the unevolved stage of the simulation ($t = 0.049$ Gyr – left-hand panel) and for the evolved one ($t = 4.018$ Gyr – right-hand panel); it was calculated in large R bins (1 kpc) along a 'slice' of the disc for each angular position considered using the SPH method; here, the patches at $\theta = 0^\circ$ are shown. The solid line represents V_c at the mid-plane, while the dashed and dot–dashed lines represent the rotation curve at $z = -1$ and $+1$ kpc, respectively. The inset at the bottom of each plot shows the zoomed-in image of the green-shaded area representing the radial position analysed in our work ($R = 8.5$ kpc) .

the expected dark matter contribution as extrapolated from the rotation curve, assuming spherical symmetry (see Section 1), namely[6] $-0.0033 \pm 0.0050\,\mathrm{M}_\odot\,\mathrm{pc}^{-3}$, leading to a slight overestimate of the dark matter density.

[6] This is just a simple average of the two cited values.

3.2.4 Assuming that the z motions are completely decoupled

The last assumption of the HF method is that the z motion is decoupled so that the distribution function of the stars is only a function of E_z. If this is true, the distribution function of the stars in the mid-plane – $f(E_z(0)) = f(w_0)$ – represents the distribution of the stars at all heights above the plane – $f(E_z(z)) = f(\sqrt{v_z^2 + 2\Phi(z)})$. Thus, it can be integrated in $w_0 = v_z(0)$ to predict the density fall-off.

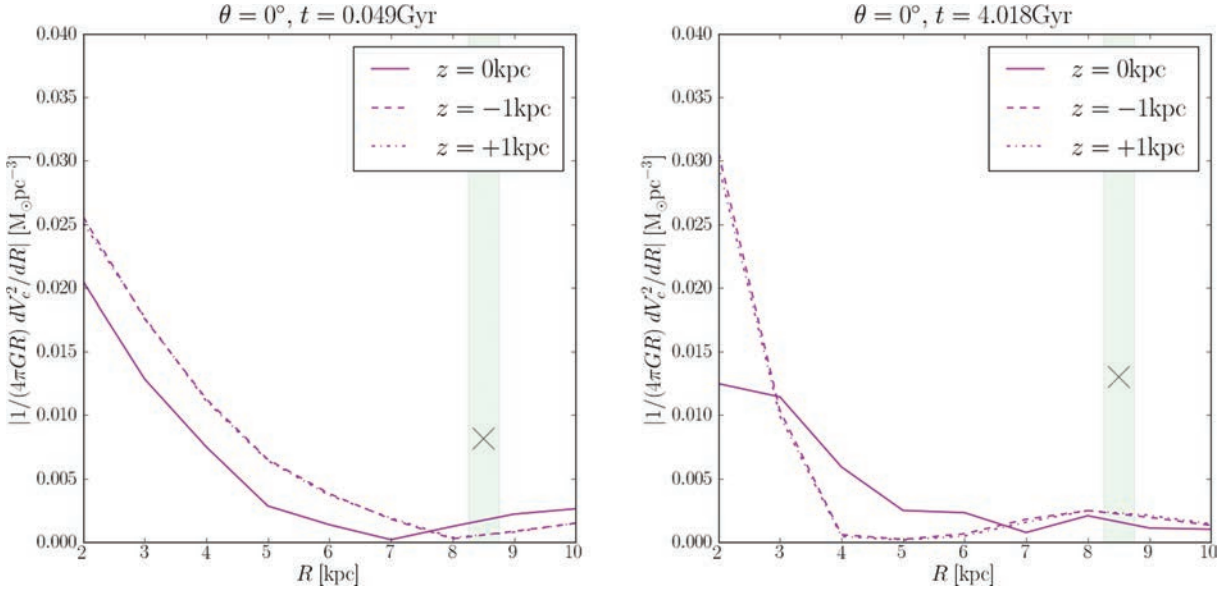

Figure 8. Absolute value of the rotation curve term, $|1/(4\pi G)\mathrm{d}V_c^2/\mathrm{d}R|$, for the unevolved stage of the simulation ($t = 0.049$ Gyr – left-hand panel) and for the evolved one ($t = 4.018$ Gyr – right-hand panel). The solid line represents the term calculated at the mid-plane, while the dashed and the dot–dashed lines correspond to $z = -1$ and $+1$ kpc, respectively. The green-shaded area represents the radial position analysed in our work (R =8.5 kpc), while the black cross gives the actual value of $\rho_{\rm dm}$ at $R = 8.5$ kpc.

In Fig. 9, we plot the distribution function at $z = 0.5$ kpc predicted from $f(w_0, 0)$ for the unevolved simulation (left-hand panel) and the evolved simulation (middle and right-hand panels representing two extreme cases at two different angular positions in the disc) in red. The actual distribution functions are overplotted in black. As expected, while for the unevolved simulation the predicted distribution function is in good agreement with the actual one (left-hand panel), the situation is different for the evolved stage. For most of the angular positions around the disc, the shape of the predicted distribution function is very different from the true one: the two volumes shown (at $\theta = 45^\circ$ and 180°) in the middle and right-hand panels represent the best and the worst cases, respectively. From this analysis, we might expect the HF method to perform well on the $\theta = 45^\circ$ patch, but poorly on the $\theta = 180^\circ$ patch. We test this expectation in Section 3.3.

Note that Statler (1989) also considered this problem. Using Stäckel potentials, he showed that E_z is a good approximation to the Galactic third integral close to the mid-plane, but not above $z \approx 1$ kpc. Two recent works by Siebert et al. (2008) and Smith, Wyn Evans & An (2009) find that the tilt of the velocity ellipsoid for the MW is indeed significant at $z \gtrsim 1$ kpc, meaning that at such height, the motion is no longer separable. In our evolved simulation, we find important non-separability even at $z \sim 500$ pc above the plane.

We also note that assuming the separability of the distribution function as $f = f(E_z)g(L_z)$, implies that $g(L_z) =$ constant with height above the mid-plane. We test this in Fig. 10, where we plot $g(L_z)$ at the mid-plane (dashed red histogram) and at $z = 0.5$ kpc (black histogram) for the unevolved (left-hand panel) and evolved simulations (middle and right-hand panel). In the unevolved disc, $g(L_z)$ at the mid-plane and $z = 0.5$ kpc are similar. For the evolved simulation,

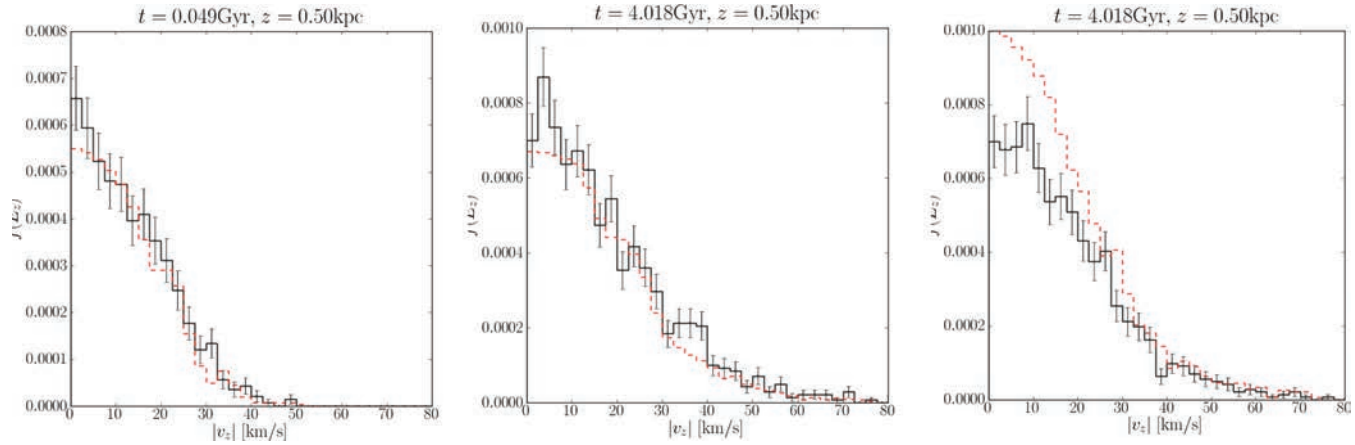

Figure 9. Distribution function above the plane at $z = 0.5$ kpc (in black) compared with the one predicted from $f(E_z(0))$ (in red). The left-hand panel represents the patch at $\theta = 0^\circ$ for the unevolved simulation ($t = 0.049$ Gyr), while the middle and right-hand panels correspond to $\theta = 45^\circ$ and 180°, respectively, in the evolved disc ($t = 4.018$ Gyr).

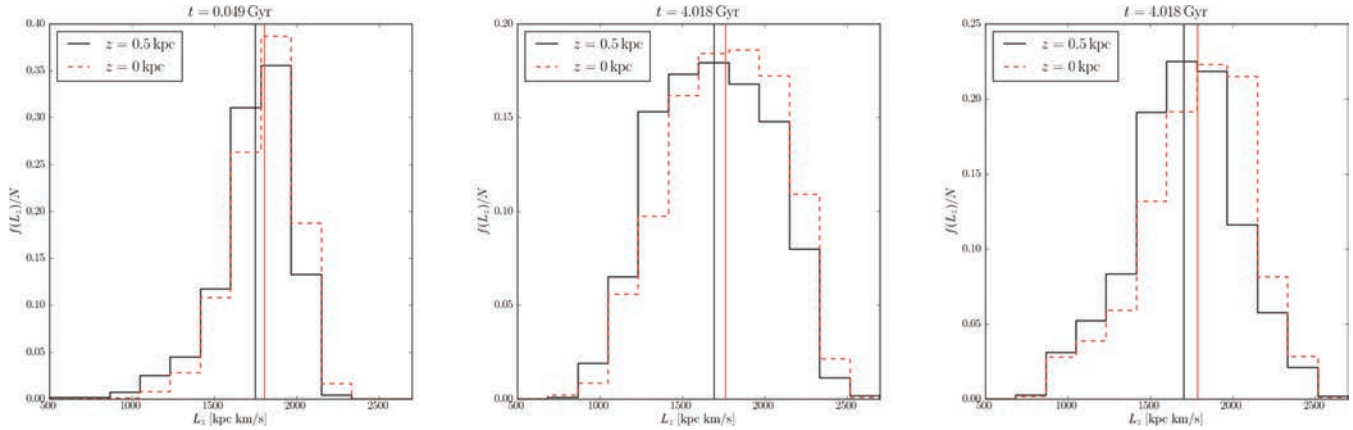

Figure 10. Angular momentum distribution $g(L_z)$ – normalized by the total number of stars N – at $z = 0$ kpc (red-dashed histogram) and at $z = 0.5$ kpc (black histogram). The red and black vertical lines represent the median of the distributions at $z = 0$ and 0.5 kpc, respectively. The left-hand panel represents the patch at $\theta = 0^\circ$ for the unevolved simulation ($t = 0.049$ Gyr), and the middle and right-hand panels correspond to $\theta = 45^\circ$ and 180° in the evolved disc ($t = 4.018$ Gyr). While the distributions have similar shapes, the mean shifts by ∼3, 4 and 5 per cent for the unevolved simulation and the evolved simulation at $\theta = 45^\circ$ and 180°, respectively. This means that the stars in the plane at 8.5 kpc have a mean guiding centre of ∼8.0 kpc, while those at $z = 0.5$ kpc have a mean guiding centres of 7.8, 7.8 and 7.7 kpc for the unevolved simulation and the evolved simulation at $\theta = 45^\circ$ and 180°, respectively.

this is not always the case. In accordance with our analysis above, the situation is better for the 'best case' $\theta = 45^\circ$ patch than for the 'worst case' $\theta = 180^\circ$ patch.

3.3 Results for the simulation

In this section, we test the MA and HF methods on our evolved and unevolved simulations. We define three different 'solar neighbourhood' patches: 36 cylinders around the disc at angular separations of 10° (represented as the red circles in Fig. 3); a 'superpatch' that is the average of the 36 cylindrical patches; and four (or eight) wedges around the disc at angles: $\theta = 0^\circ, 90^\circ, 180^\circ$ and 270° (and additionally $45^\circ, 135^\circ, 225^\circ$ and 315° for the evolved simulation which is not axisymmetric, to examine all the relevant positions with respect to the bar). All patches are represented as the red shaded areas in Fig. 3. The cylinders have sampling similar to the currently available *Hipparcos* data that we consider in Section 4. The 'superpatch' gives sampling equivalent to that expected from the *GAIA* mission (*GAIA* will obtain distances with an accuracy better than 0.1 per cent for ∼100 000 stars within 80 pc, Bailer-Jones 2008). However, we can only apply the superpatch to the unevolved simulation that is axisymmetric. For this reason, we introduce also the wedges that contain approximately five times the number of stars in a cylinder; they are the best compromise to obtain larger sampling for a sufficiently local volume in the non-axisymmetric disc. Note that, for the unevolved disc, the cylinders and wedges tell us only about sampling errors since the disc is axisymmetric (the results for each patch should be statistically equivalent). For the evolved disc, however, the different patches explore the effect of spiral structure and disc inhomogeneities on our analysis.

We consider a single visible component to build the mass model for the disc, described by its density in the plane and its velocity dispersion. We set the Sun's position at $R_\odot = 8.5$ kpc. We let the local dark matter density ρ_{dm} vary in the range $[0, 1]\,M_\odot\,pc^{-3}$ and the disc mass density $\rho_s(0)$ in the range $\pm 0.014\ M_\odot\,pc^{-3}$ around the actual value that we measure for the simulation. This range has a width comparable to the observational uncertainties for the data we consider in Section 4 (see also Table 4).

For the HF method, we need the distribution function in the mid-plane, $f(w_0)$, to be used in equation (18). To compute this, we fit the velocity distribution of stars with $|z| \leq 50$ pc (see Section 3.3.1.1) with a Gaussian function for the unevolved simulation and a double Gaussian for the evolved one (an example fit is shown in the left-hand panel of Fig. 2).

3.3.1 The unevovled simulation

We first consider the unevolved simulation ($t = 0.049$ Gyr) that fulfils the hypotheses of the methods.

3.3.1.1 Maximum volume of the patch. We first consider the appropriate size of the volume for the MA method: it should be small enough in the radial direction (ideally infinitesimal) to average the potential and its derivatives over R to solve the Jeans equation for a one-dimensional slab. Of course, we need a large patch for the best possible sampling. In this section, we use the unevolved simulation to measure how large our patch can be before systematic errors dominate over our sample error. For this, we use the 'superpatch' described in Section 3.3 above. We consider the average of 36 cylinders around the disc at $R_\odot = 8.5$ kpc with radii $R = 150$, 250, 300, 400 and 500 pc.

In addition, the HF method requires measuring the distribution function in the mid-plane: $f(w_0)$. For this, we must choose a vertical scale to determine $f(w_0)$, and again there is a trade-off between bias and sample error. To find the optimal height, we compute the velocity distribution considering star particles up to $|z| < 50$, 75 and 100 pc. Note that for any patch size, there will be a bias error due to the finite volume considered. Here we find the largest patch size (for '*GAIA*' sampling; the 'superpatch' described in Section 3.3) for which the bias error is small compared to the sample error. If the sampling for a given volume is improved, then we will become more sensitive to bias. In this case, the optimal patch size will be smaller than that found here.

For each choice of R and $|z|$, we apply our MCMC method to explore the ρ_s–ρ_{dm} parameter space and calculate χ^2 for each model.

Table 3. Best χ^2 for different sizes of the 'local volume' box; $|z| <$ 50, 75, 100 pc is the height used to construct the mid-plane velocity distribution; $R = 150, 250, 300, 400$ and 500 pc is the radial size of the cylindrical box. The dashes correspond to a failure of the MCMC in recovering the density, that is, it cannot find an acceptable value.

	$R = 150$ pc	250 pc	300 pc	400 pc	500 pc
$\|z\| < 50$ pc	1.16	1.96	2.52	3.60	–
$\|z\| < 75$ pc	1.21	2.18	3.04	5.03	–
$\|z\| < 100$ pc	–	–	–	–	–

We first apply our MA method to test the optimal radial extent of a patch. For a cylinder of radius $R > 500$ pc, the MCMC fails to find a solution, indicating that the bias errors are dominant. For smaller patches, we recover the correct values of ρ_s and ρ_{dm} within our quoted errors, but find that the best χ^2 shrinks with R. Next, we apply the HF method. In this case, the MCMC fails to find a solution if the mid-plane velocity distribution is averaged up to $|z| = 100$ pc. The best χ^2 values for each case are reported in Table 3 (the situation for the MA method is very similar to the first line). The recovered densities in the different volumes are shown in Fig. 11: for $R = 250, 300$ and 400 pc, and when we calculate the velocity distribution function in the mid-plane using stars with $|z| < 50$ pc, we always recover the correct answer even if the agreement between the predicted and the measured density fall-off of the tracers give rise to increasing χ^2 values with R. For $R = 150$ pc, the result is not as good, likely owing to the poorer sampling. Calculating the velocity distribution in the mid-plane from stars with $|z| < 75$ pc always gives slightly biased results.

Given the above results, we will consistently use patches with $R =$ 250 pc and average our mid-plane velocity distributions for stars with $|z| < 50$ pc. This volume is similar to that used by Holmberg & Flynn (2000) whose data we consider in Section 4.

3.3.1.2 Degeneracy in ρ_s and ρ_{dm}. In their work, Holmberg & Flynn (2000) fit the density fall-off of the stellar tracers up to 0.1–0.2 kpc which approximately corresponds to the MW disc half-mass scaleheight $z_{1/2}$. If we adopt the same criteria for our 'superpatch', we see that the area of the ρ_s–ρ_{dm} plane explored by the MCMC corresponds to a 45° stripe with almost the same value of χ^2 for all models. This means that we have a nearly flat distribution of models and a strong degeneracy between ρ_s and ρ_{dm}. This is shown in the left-hand panel of Fig. 12. The grey contours represent the density of models explored by the MCMC, while the black contour contains all models with $\chi^2 \leq 1.1\chi^2_{best}$.

This strong degeneracy means that we can only determine the total density on the plane $\rho_{tot}(0) = \rho_s(0) + \rho_{dm}(0)$, but not ρ_s and ρ_{dm} separately. To break this degeneracy – and obtain smaller error bars – we must fit the tracers to higher z. This has been noted in earlier work. Bahcall (1984c) state that data up to $z = 600$ pc are required to be sensitive to the SHM dark matter density.

In the right-hand panel of Fig. 12, we show our recovered ρ_s and ρ_{dm}, but now fitting to $|z| = 0.75$ kpc (approximately four times $z_{1/2}$). This is sufficient to break the degeneracy and we recover the correct answer for both ρ_s and ρ_{dm} inside our 1σ error bars. We show results here for brevity only for the MA method; however, the HF method produces similar results for this test. For the rest of our analysis, we will fit the density fall-off of the tracers up to 0.75 kpc.

3.3.1.3 Introduction of realistic errors. As already stressed, the 'superpatch' has statistics comparable to that expected for the *GAIA* mission. In this section, we consider the effect of realistic observational errors in the velocities and positions of the stars on the recovered stellar and dark matter densities.

We consider errors typical for current *Hipparcos* data (that we consider in Section 4) and *GAIA* quality data. The *Hipparcos* mission provided $\sim 10^4$ stars out to $\sim$100 pc with proper motions and parallaxes accurate to <10 per cent (Dehnen 2002). In Holmberg & Flynn (2000), the (incomplete) radial velocity information from *Hipparcos* data was ignored and the velocity distribution was computed using only low-latitude stars, whose motion is dominated by the proper motion. The confidence limits were estimated via a series of Monte Carlo simulations of observations drawn from synthetic *Hipparcos* survey catalogues, taking into account the *Hipparcos*

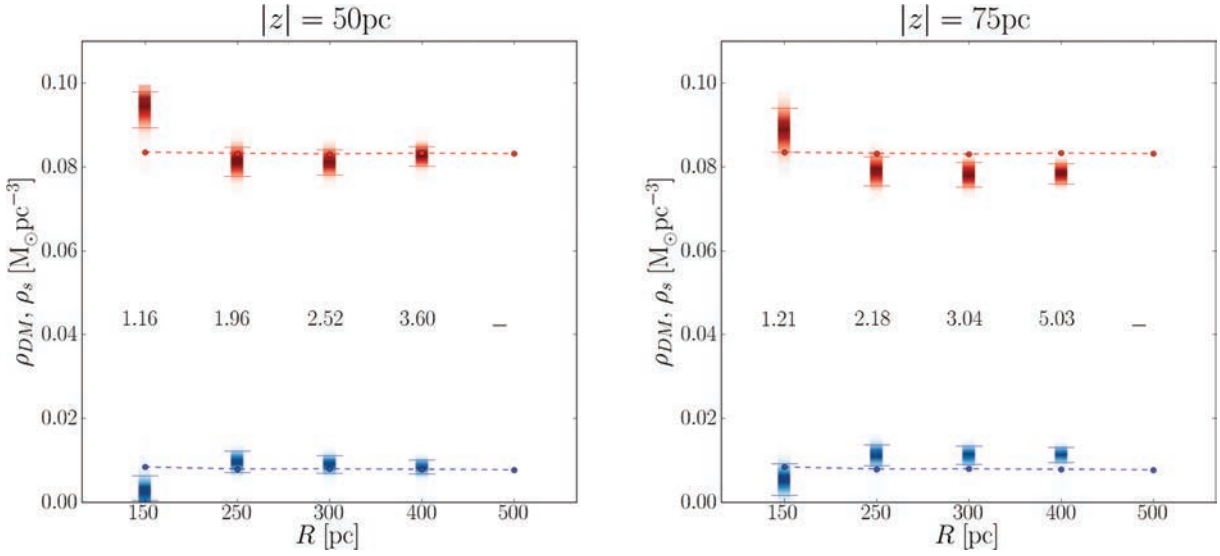

Figure 11. Models explored by the MCMC for the HF method, using different sizes of the 'local volume' box. The left-hand (right-hand) panel corresponds to the velocity distribution in the mid-plane constructed using stars with $|z| < 50$ pc ($|z| < 75$ pc). On the x-axis, the different radial sizes are indicated. The blue (red) shaded rectangles represent the recovered dark (visible) matter density. The blue (red) dashed line and filled dots represent the actual value of ρ_{dm} (ρ_s). The horizontal red (blue) segments represent the 90 per cent errors in the recovered value of ρ_s (ρ_{dm}).

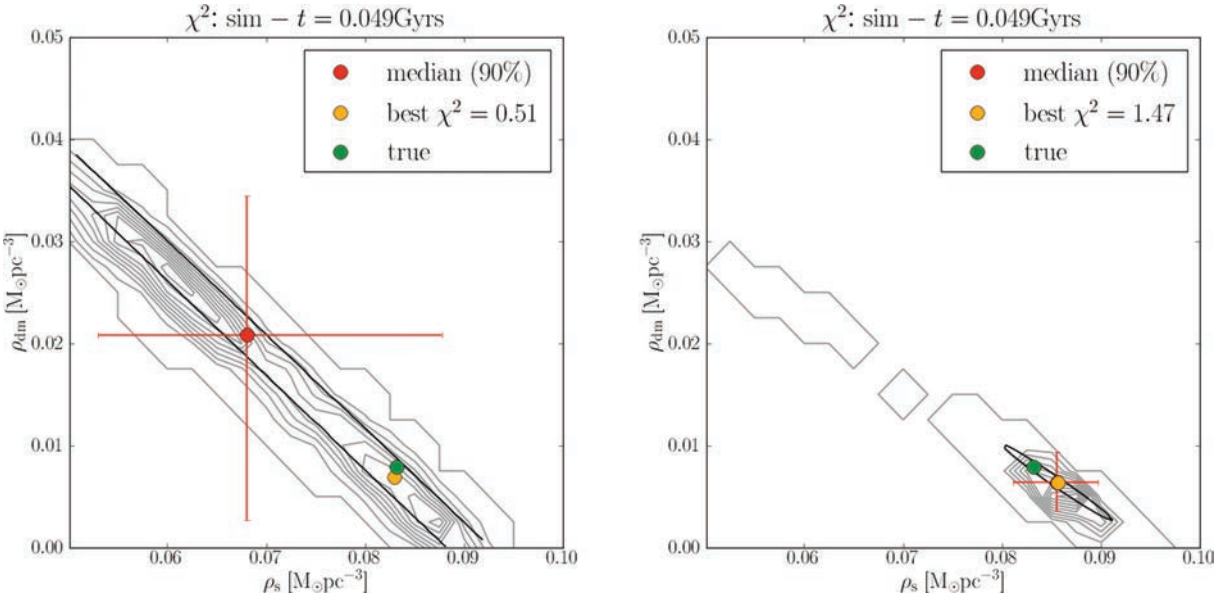

Figure 12. MCMC models in the ρ_s–ρ_{dm} space for the 'superpatch' applied to the unevolved simulation. The yellow dot corresponds to the best χ^2_{best} model; the green dot corresponds to the true value; the red dot is the median of the distribution with 90 per cent error bars; the black contours contain all models with $\chi^2 \leq 1.1\chi^2_{best}$; and the grey contours represent the density of models explored by the MCMC. Left-hand panel: fitting the density fall-off up to $|z| = 0.25$ kpc ($\gtrsim z_{1/2}$); right-hand panel: fitting up to $|z| = 0.75$ kpc ($\gtrsim 4z_{1/2}$).

magnitude limits and magnitude-dependent parallax and proper-motion errors. For the A and the F samples, they found a 95 per cent confidence limit of ± 0.011 and ± 0.023 M$_\odot$ pc^{-3}, respectively.

GAIA will determine distances for 150 million stars with an accuracy better than 10 per cent (within 8 kpc) and some 100 000 stars to better than 0.1 per cent within 80 pc (Bailer-Jones 2008). For an unreddened K giant at 6 kpc, *GAIA* will measure the distance accurate to 2 per cent and the transverse velocity with an accuracy of about 1 km s^{-1} (Bailer-Jones 2008).

To understand the impact of *GAIA*'s accuracy, we introduce Gaussian errors in the velocity of 1 km s^{-1} and an accuracy in the positions of 2 per cent. We then run our MCMC chain on these input data with errors. We find that our recovered values for the density are unchanged, but χ^2 increases. We conclude that velocity–position errors are a perturbation on sample errors and model systematics.

Here we included only uncorrelated errors on distances and velocities of the stars; correlated errors could be a concern when one calculates space velocity from proper motions. However, in the methods considered, only the vertical velocity of stars in a small volume (i.e. mostly high-latitude stars) for which v_z is mostly due to the radial velocity is considered. In addition, we show that the main uncertainties come from the model rather than measurement uncertainties.

3.3.1.4 The importance of statistics. In this section, we investigate the effect of sample size. We considered a *GAIA* data-quality mission with 'superpatch' sampling. Now we consider smaller patches with sampling more similar to *Hipparcos* data. Good statistics are particularly important for the HF method that requires the shape of the in-plane velocity distribution function rather than just its moments.

We consider four cylindrical volumes around the disc with statistics comparable to *Hipparcos* data (∼2000–3000 within $|z| < 200$ pc) and four wedge-shaped larger volumes at the same angular positions, having the same radial and vertical size, but covering a larger azimuthal angle (and containing about four to five times more particles).

The results are reported in Fig. 13, which shows the models explored by the MCMC for the MA method for the four cylinders (left-hand panel) and the four wedges (right-hand panel). In both cases, the method recovers the correct values for ρ_s and ρ_{dm} within our quoted errors, with the error bars shrinking with improved sampling as expected. The results are almost identical for the HF method for this early stage of the simulation.

3.3.2 *The evolved simulation*

3.3.2.1 The HF method. In the previous section, we demonstrated that the MA and HF methods perform equivalently well when applied to the ideal situation of an isothermal axisymmetric disc, fulfilling all the standard assumptions. Both recover the local dark matter and mid-plane stellar densities within our quoted uncertainties. The situation is different when we consider the evolved stage of the simulation. The onset of spiral arms and a bar causes significant radial mixing that induces vertical non-isotropy and non-separability that violate key assumptions in the HF method. As such, we might expect its performance to degrade accordingly.

We consider eight different wedges[7] around the evolved disc to sample patches that lie on/away from spiral/bar features. We first apply the HF method, assuming an isothermal disc mass model. The results are shown in Fig. 14 (upper panel). As expected, we do not recover the correct value of the local stellar and dark matter densities for most of the volumes. The possible reasons are (i) the neglected non-isothermality of the disc; (ii) the unsatisfactory fit of the distribution function with a double Gaussian (at least for some

[7] In order not to confuse sampling errors with systematic errors, we show the results for the evolved simulation only for the wedges. The results for the MA method applied to the cylinders are given in Appendix C.

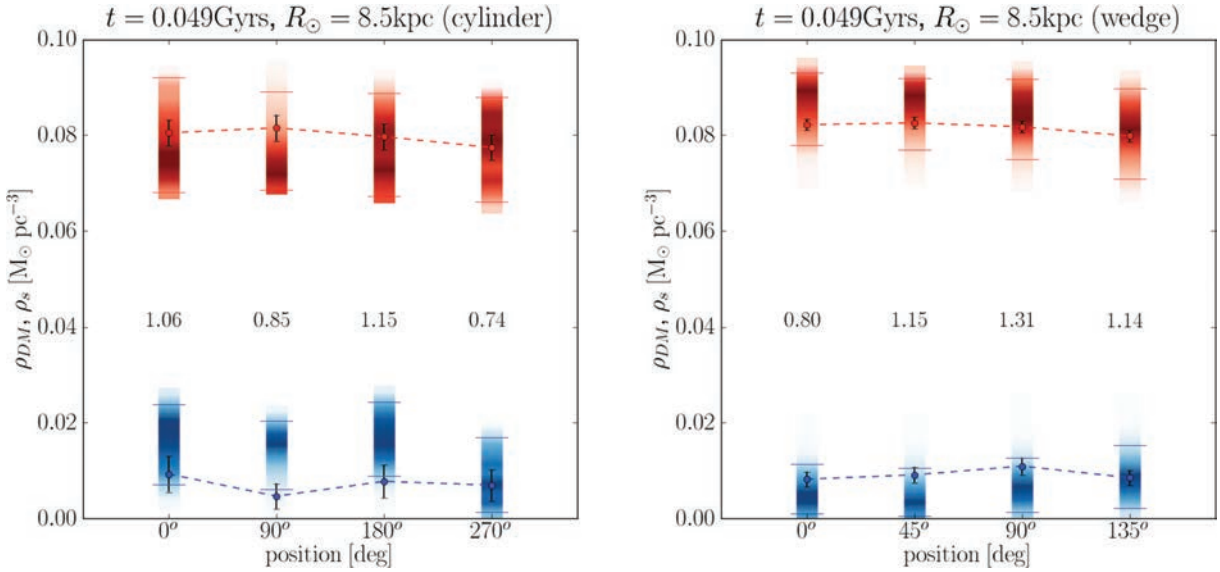

Figure 13. Models explored by the MCMC for the MA method for the four cylinders (left-hand panel) and the four wedges (right-hand panel) represented as shaded areas of different colours. Blue corresponds to the recovered dark matter density $\rho_{\rm dm}$ and red to the recovered visible matter density $\rho_{\rm s}$ in the plane. The filled dots represent the corresponding actual values with Poisson errors. The red and blue horizontal segments show the 90 per cent errors on the recovered densities. The numbers correspond to the reduced χ^2 values. Note that the apparent fluctuations in density at different angular positions are due to the sample noise.

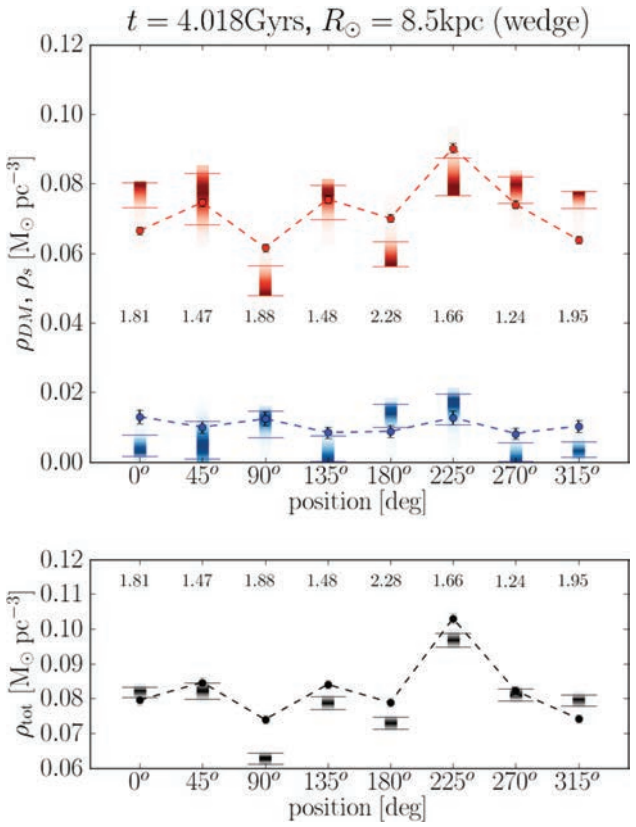

Figure 14. Models explored by the MCMC for the HF method, assuming isothermality of the disc population and using a double Gaussian fit of the velocity distribution for the eight wedge-shaped solar neighbourhood volumes at $R = 8.5$ kpc. Upper panel: recovered dark and visible matter density (the symbols and colours are as in Fig. 13). Lower panel: recovered total (dark+visible) matter density. The numbers under each stellar density are the reduced χ^2 for the best-fitting model.

of the volumes considered); and (iii) at this stage of the simulation, the distribution function of the stars above the plane is not well represented by the distribution in the mid-plane.

To test the first two possible sources of error, we correct for the non-isothermality of the disc population using equation (9) instead of equation (15), and we interpolate linearly the distribution function instead of fitting it. The results are very similar; the reason for such a small change is that it is the non-isothermality of the *tracers* that really matters, not that of the whole disc model. (Recall that the HF method does not assume that the tracers are isothermal, but rather that their distribution function is a function only of the vertical energy E_z.) Thus, we can conclude that it is the assumption that $f = f(E_z)$ that leads to the systematic bias in the recovery of $\rho_{\rm dm}$ and $\rho_{\rm s}$ for the HF method applied to the evolved simulation. To see this, consider the wedges at $\theta = 45^\circ$ and 180°. Recall from Section 3.2 that for the former wedge, the velocity distribution at $z = 0.5$ kpc was well predicted from $f(w_0)$, while for the latter wedge, the velocity distributions differed strongly. As might be expected, the $\theta = 45^\circ$ wedge gives an excellent recovery for $\rho_{\rm dm}$ and $\rho_{\rm s}$, while the $\theta = 180^\circ$ wedge gives a very poor recovery. In the lower panel of Fig. 14, the recovered total (visible+dark) matter density is shown: the HF method fails to recover the correct answer in many cases, even dramatically (e.g. see $\theta = 90^\circ$ or $\theta = 315^\circ$).

The above is a problem for the HF method – and indeed any method that assumes that $f = f(E_z)$ – if such methods are applied at heights larger than ∼1 disc scaleheight. However, going to this height is necessary to break the degeneracy between $\rho_{\rm dm}$ and $\rho_{\rm s}$ (Section 3.3.1.2). It may be possible to build an unbiased distribution function (or mixed) method that works at large height above the disc plane, by using more complex forms for f. This is beyond the scope of this work.

3.3.2.2 The MA method. We first apply the MA method, assuming isothermality of the tracers to the eight wedges. The results are shown in Fig. 15. Note that, similar to the HF method, the density recovery in all of the wedges is systematically biased and poor. The

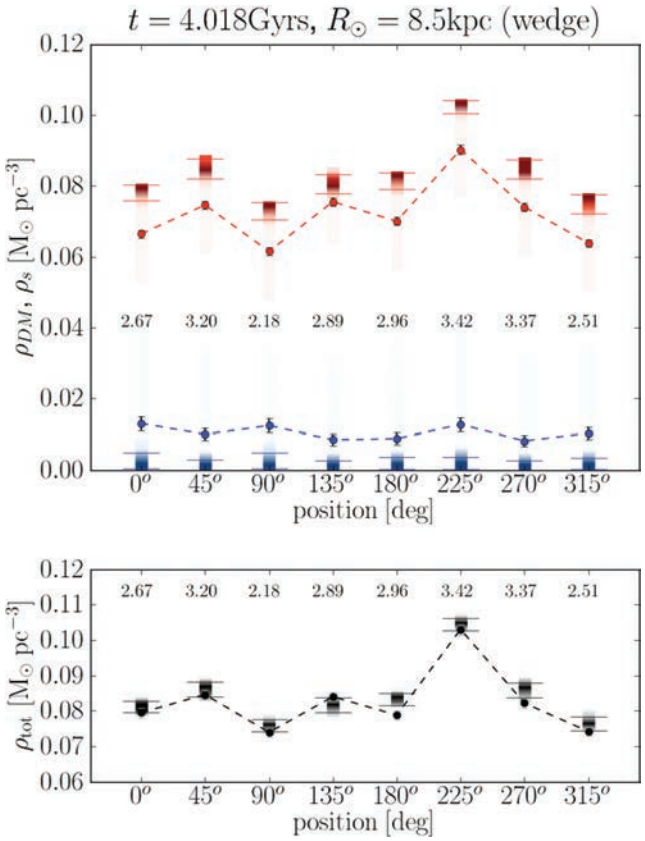

Figure 15. Models explored by the MCMC for the MA method, assuming isothermality for eight wedge-shaped solar neighbourhood volumes at $R = 8.5$ kpc. The symbols and colours are as in Fig. 14. The numbers under each stellar density are the reduced χ^2 for the best-fitting model.

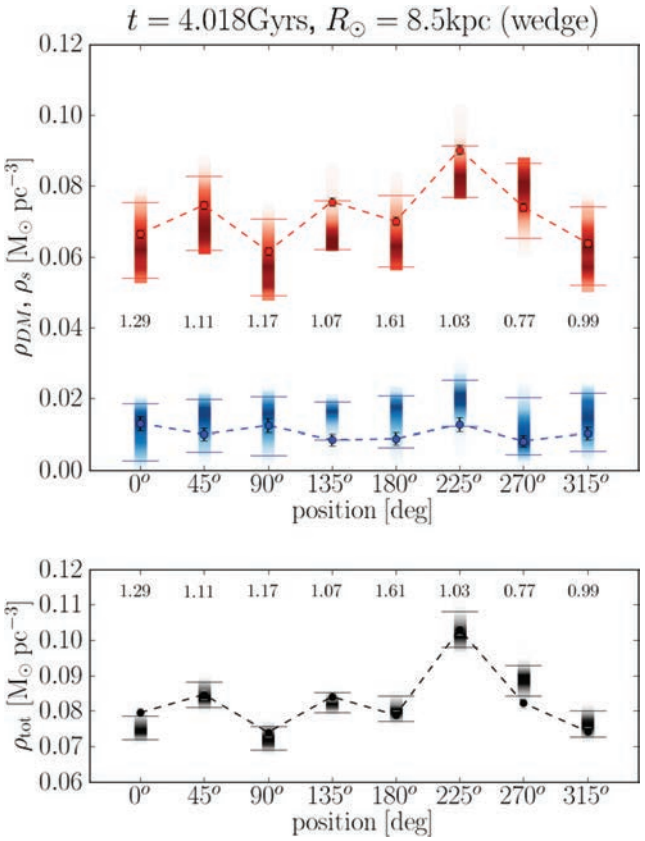

Figure 16. Models explored by the MCMC for the MA method for eight wedge-shaped solar neighbourhood volumes of the evolved simulation at $R = 8.5$ kpc. Upper panel: recovered values of the dark and visible matter density. Lower panel: recovered values of the total (dark+visible) matter density. The symbols and colours are as in Fig. 15.

MCMC explores a very small area in the ρ_s–ρ_{dm} parameter space, always pushing on the lower limit imposed for ρ_{dm}. The error in this case has a particular direction: this probably owes to the deviation from zero of the sum of the second and third terms of the Jeans equation (represented as a grey line in Fig. 6). When we assume isothermality, this has a particular sign.

Next, we include the non-isothermality of our tracers. The results are shown in Fig. 16. Our results are now excellent for all patches, recovering the correct unbiased value for both ρ_{dm} and ρ_s (and the total matter density) within our quoted 90 per cent uncertainties. This emphasizes the importance of knowing $\overline{v^2_{z,i}}(z)$ precisely for each tracer population. In fact, a small deviation from the actual velocity dispersion of the tracers is enough to lead to a wrong result; for this reason, we linearly interpolate $\overline{v^2_{z,i}}(z)$. Note that this is possible for the simulation if we consider large enough wedges, so that the velocity dispersion is quite smooth. For real data, the situation is more complicated since we have to deal with velocity uncertainties and noisier velocity dispersions. In this case, we can use the MCMC to marginalize over such uncertainties. We demonstrate this for the evolved simulation in Appendix C.

Note, however, that the errors are still large even though the relative amount of dark matter in the simulation is larger than we expect in the MW. We can further improve on this if the errors on $\rho_s(0)$ can be reduced. We explore this in Fig. 17 where we assume that $\rho_s(0)$ is known to an accuracy of $\pm 0.007\,M_\odot$ pc^{-3} instead of $\pm 0.014\,M_\odot$ pc^{-3} as previously assumed. The results are correspondingly improved, as expected. This suggests that the key limiting factors to determining ρ_{dm} are a good measure of the non-isothermality of the tracer population, and an accurate determination of the local visible matter density.

4 APPLICATION TO REAL DATA

In this section, we illustrate the power of our new MA method by applying it to the *Hipparcos* data used by Holmberg & Flynn (2004) to calculate the local surface density up to $z = 0.7$ kpc. As we demonstrated in Section 3.3.1.2, fitting the density fall-off up to large z is required to break the degeneracy between ρ_s and ρ_{dm}.

4.1 The data

We use the raw data of the 'HD sample' (Holmberg & Flynn 2004) from Chris Flynn (private communication) consisting of 139 K giants from Flynn & Freeman's (1993) catalogue in a cone pointing towards the South Galactic Pole with an aperture of 430 deg^2, having a limiting visual magnitude of $V = 9.2$, a magnitude range of $0.0 < M_V < 2.0$ and a colour range of $1.0 < B - V < 1.5$ (see fig. 11, upper panel, in Holmberg & Flynn 2004). Holmberg & Flynn (2004) compute the velocity distribution of the tracers using a volume-complete (to 100 pc) sample of 395 K stars from the *Hipparcos* catalogue with radial velocity information (in the same colour and absolute magnitude ranges). Because of the nature of those data, the analysis is more complicated and uses the *Hipparcos* luminosity function for K giants (see fig. 2 in Holmberg & Flynn

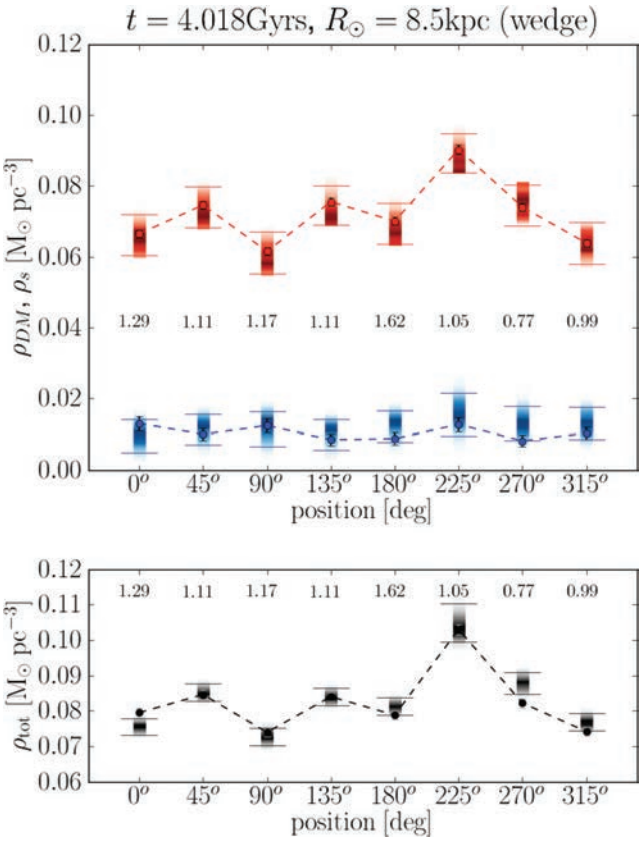

Figure 17. Models explored by the MCMC for the MA method for eight wedge-shaped solar neighbourhood volumes of the evolved simulation at $R = 8.5$ kpc. In this case, tighter constraints on ρ_s are assumed (an error of $\pm 0.007\,M_\odot\,pc^{-3}$ instead of $\pm 0.014\,M_\odot\,pc^{-3}$). The symbols and colours are as in Fig. 15.

2004). A further complication as compared to our simulation data is the mass model for the real MW which has several gas and stellar components, each with its local density and velocity dispersion. The density in the mid-plane, $\nu_{i,0}$, and the velocity dispersion, $\overline{v_{z,i}^2}(0)$, of the various visible components (Flynn et al. 2006) are listed in Table 4.

The HD sample contains very few stars, so we also include additional constraints from the literature. This illustrates the power of our MA technique coupled to the MCMC since additional constraints are straightforward to add. As additional data, we include the two volume-complete samples of stars from *Hipparcos* data employed by Holmberg & Flynn (2000) in their calculation of the local density: the A star sample (including B5 to A5 stars) which contains 2026 stars in a cylinder with radius and height of 200 pc and the F sample (A0 to F5) which comprises 3080 stars within 100 pc. We also ensure that the surface density calculated for each model explored by the MCMC agrees with the observational constraints. In the second column of Table 4, the current observational constraints for the surface densities of the different visible components are listed. From the values in this table, we adopt a total visible surface density for the disc of $\Sigma_{vis}(R_\odot) = 49.4 \pm 4.6\,M_\odot\,pc^{-2}$. For each model explored by the MCMC, we then calculate the expected surface density as

$$\Sigma_s^{exp} = 2\int_0^\infty \rho_s(z)dz = 2\int_0^\infty \sum_i \nu_{i,0} \exp\left(-\frac{\Phi(z)}{\overline{v_{z,i}^2}}\right) dz, \qquad (24)$$

Table 4. The disc mass model taken from Flynn et al. (2006). Each component in the table gives the local mass density in the mid-plane, $\rho(0)$, in $M_\odot\,pc^{-3}$, the total column density Σ in $M_\odot\,pc^{-2}$ and the vertical velocity dispersion $\overline{v_{z,i}^2}(0)^{1/2}$ in $km\,s^{-1}$. Uncertainties on the densities are of the order of 50 per cent for all the gas components (indicated with *) and 10–20 per cent for all the stellar components. For the thick disc, the column density is rather well known, while the velocity dispersion and the volume density are poorly known such that they should have larger error bars. However, these two quantities are essentially nuisance parameters for our analysis here. Since they anticorrelate and – as pointed out by Kuijken & Gilmore (1989c) – the local gravitational potential is mainly constrained by the column density, we simply assume small errors for both here such that the integrated column agrees with the observed value.

Component	$\nu_{i,0}(0)$ ($M_\odot\,pc^{-3}$)	Σ_i ($M_\odot\,pc^{-2}$)	$\overline{v_{z,i}^2}(0)^{1/2}$ ($km\,s^{-1}$)
H_2^*	0.021	3.0	4.0 ± 1.0
HI(1)*	0.016	4.1	7.0 ± 1.0
HI(2)*	0.012	4.1	9.0 ± 1.0
Warm gas*	0.0009	2.0	40.0 ± 1.0
Giants	0.0006	0.4	20.0 ± 2.0
$M_V < 2.5$	0.0031	0.9	7.5 ± 2.0
$2.5 < M_V < 3.0$	0.0015	0.6	10.5 ± 2.0
$3.0 < M_V < 4.0$	0.0020	1.1	14.0 ± 2.0
$4.0 < M_V < 5.0$	0.0022	1.7	18.0 ± 2.0
$5.0 < M_V < 8.0$	0.007	5.7	18.5 ± 2.0
$M_V > 8.0$	0.0135	10.9	18.5 ± 2.0
White dwarfs	0.006	5.4	20.0 ± 5.0
Brown dwarfs	0.002	1.8	20.0 ± 5.0
Thick disc	0.0035	7.0	37.0 ± 5.0
Stellar halo	0.0001	0.6	100.0 ± 10.0

where $\Phi(z)$ is the potential computed according to the parameters of the model. We then compare this with $\Sigma_{vis}(R_\odot)$, including the result in our determination of χ^2 for each model.

As parameters to fit in the MCMC, we use (1) the local dark matter density ρ_{dm}; (2) the total visible density in the mid-plane $\rho_s(0)$; (3) the relative fractions of the visible components $\nu_{i,0}/\rho_s(0)$; (4) their velocity dispersions in the mid-plane $\overline{v_{z,i}^2}(0)^{1/2}$; (5) the velocity dispersion as a function of z of the tracers; and (6) the normalization of the density fall-off of the tracers. We allow the densities and the velocity dispersions of the different components to vary within their measured uncertainties (the errors for each component are given in Table 4). We let the total visible density in the plane, $\rho_s(0)$, to vary within its observed range, $\rho_s(0) = 0.0914 \pm 0.0140\,M_\odot\,pc^{-3}$, and the dark matter density to vary between 0 and $0.5\,M_\odot\,pc^{-3}$. The velocity dispersion of the tracers in the mid-plane is given by the Gaussian fit of the velocity distribution calculated by Holmberg & Flynn (2004), namely $\overline{v_{z,i}^2}(0)^{1/2} = 18.3 \pm 0.6\,km\,s^{-1}$ for the HD sample, and by Holmberg & Flynn (2000), that is, $\overline{v_{z,i}^2}(0)^{1/2} = 5.7 \pm 0.2\,km\,s^{-1}$ for the A sample and $\overline{v_{z,i}^2}(0)^{1/2} = 8.3 \pm 0.3\,km\,s^{-1}$ for the F sample.

After computing the expected density fall-off for the tracers of the (magnitude-limited) HD sample through equation (8), we apply the *Hipparcos* luminosity function and the magnitude cut $V < 9.2$ to compare it with the observed number of stars in the cone. The A and F samples from Holmberg & Flynn (2000) are easier to fit, since they are volume complete.

Unfortunately, we do not have much information about the velocity dispersion above the plane of the different disc components included in the mass model. As such, we consider two extreme assumptions: one in which all of the visible components of the disc

and the tracers are isothermal; and another in which the tracers and all of the visible components of the disc are non-isothermal. We model the non-isothermality of the stars in the second case, assuming a behaviour similar to the fit by Bond *et al.* (2010) to blue disc stars. We proceed in the following way:

(i) We use the velocity dispersion in the plane of each component, $\overline{v^2_{z,i}}(0)^{1/2}$, with its error bar (see Table 4) and the constants $A = 4 \pm 0.8$ and $b = 1.5 \pm 0.2$ calculated by Bond to compute the velocity dispersion for that particular species at the maximum fitted height, $z_{\rm max}$, with the help of Bond's fitting function:

$$\overline{v^2_{z,i}}(z_{\rm max})^{1/2} = \overline{v^2_{z,i}}(0)^{1/2} + A|z_{\rm max}/{\rm kpc}|^b. \quad (25)$$

(ii) Since the function fitted by Bond is discontinuous at $z = 0$, we use a quadratic function:

$$\overline{v^2_{z,i}}(z) = \overline{v^2_{z,i}}(0)(1 + C|z|^2). \quad (26)$$

We choose the parameter C of equation (26) so that the quadratic passes through $\overline{v^2_{z,i}}(0)$ and the value of $\overline{v^2_z}(z_{\rm max})$.

In Fig. 18, the quadratic curve (red solid line) and the Bond-like fit (red dotted line) for the HD tracers are shown. The shaded red area represents the uncertainties on Bond's fit due to the errors in A and b calculated by Bond *et al.* (2010) and the uncertainties in $\overline{v^2_{z,i}}(0)^{1/2}$ (blue point). Note that the quadratic function obtained is very close to Bond's fit and lies inside its quoted uncertainties.

We stress that the velocity dispersion law from Bond *et al.* (2010) refers to different types of stars that are hotter than the A, F and K stars we consider here. However, recall that our goal is simply to explore the effect of varying the functional form of $\overline{v^2_{z,i}}$.

To summarize, our approach is as follows: (i) we use the mass model of Table 4 (with a constant dark matter contribution) to calculate the potential; (ii) we use this potential and an isothermal/Bond-like velocity dispersion law (separately normalized for each tracer population) to predict the density fall-off of the three tracer populations; (iii) we simultaneously predict the total visible surface density; and (iv) from the comparison of the three predicted and observed density laws (and the predicted and observed visible surface densities), we accept or discard the initial guess for the potential at each iteration of the MCMC.

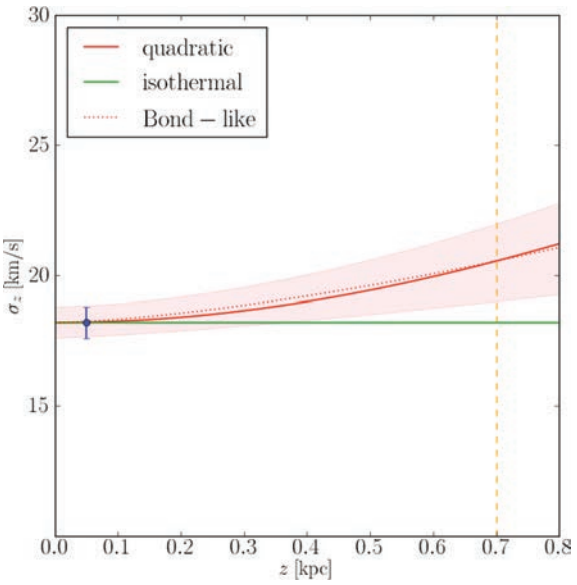

Figure 18. Bond-like (dotted red line), quadratic (red solid line) and isothermal (solid green line) velocity dispersion functions for the 'HD sample'. The red-shaded area represents the errors in the Bond-like function. The blue dot represents the measured velocity dispersion in the local sample ($|z| <$ 100 pc) and the dashed orange line is at $z = 0.7$ kpc (the upper z limit for the HD sample).

The application of the MA method, assuming isothermal or Bond-like velocity dispersion profiles, leads to very different results for the recovered visible and dark matter densities, but with a very similar value of χ^2. The results are given in Fig. 19. The recovered visible and dark matter densities calculated with the MA method, assuming isothermality (upper panel) and Bond-like non-isothermality (lower panel), are shown. The red dot represents the median of the distribution of the models explored by the MCMC in the $\rho_{\rm s}$–$\rho_{\rm dm}$ plane within a 90 per cent confidence interval. The blue dashed lines correspond to the priors imposed on $\rho_{\rm s}$; the purple stripe shows the result by Holmberg & Flynn (2000); and the green and yellow horizontal dashed lines represent the lower limit of the local dark matter density ($\simeq 0.005\,{\rm M}_\odot\,{\rm pc}^{-3}$) as extrapolated from the MW's rotation curve (a summary of these values is given in Table 5) and the SHM canonical value ($\simeq 0.008\,{\rm M}_\odot\,{\rm pc}^{-3}$), respectively.

If all of the stellar tracers are assumed to be isothermal, we obtain a fit similar to Holmberg & Flynn (2000) with a dark matter density of $0.006^{+0.008}_{-0.005}\,{\rm M}_\odot\,{\rm pc}^{-3}$. By contrast, if we assume instead a 'Bond-like' non-isothermality for the stellar populations in the disc, the recovered dark matter density is much larger ($0.036^{+0.007}_{-0.008}\,{\rm M}_\odot\,{\rm pc}^{-3}$); the measured local dark matter densities, corrected for the rotation curve using the Oort constants (see Section 3.2.3), are $0.003^{+0.009}_{-0.007}\,{\rm M}_\odot\,{\rm pc}^{-3}$ (for the isothermal tracers) and $0.033^{+0.008}_{-0.009}\,{\rm M}_\odot\,{\rm pc}^{-3}$ (for non-isothermal tracers). They are represented by the black dots in Fig. 19.

Yet the (non-reduced) χ^2 for both models is comparable: $\chi^2 = 41.5$ for the fully isothermal model and $\chi^2 = 42.3$ for the non-isothermal model. This means that, for the data we consider here, we cannot discriminate between these two scenarios. Note that our χ^2 values seem rather high (similar to those for the model fits in Holmberg & Flynn 2000). The number of fitted parameters is 38, using 39 data points and two additional constraints (the total visible density and the surface density). The latter constraint is non-linear and so we cannot simply compute a reduced χ^2. However, assuming that this constraint enters linearly, this gives the remaining 3 degrees of freedom and a reduced χ^2 of 13.8 for the isothermal model and 14.1 for the non-isothermal model. This is still high, suggesting that our models are a poor representation of the data, despite the apparent goodness-of-fit (shown in Fig. 20). The reason for this is that our method leads by construction to a smooth density fall-off which cannot account for the (statistically significant) wiggles present in the analysed samples.

Finally, we repeated our analysis using the isothermal mass model of Table 4, but still assuming a Bond-like non-isothermal velocity dispersion for the tracers. We found that the result remained almost unchanged. This means that the method is very sensitive to the velocity dispersion of the tracer population that must be known accurately. However, the visible components of the mass model are less important. This is not surprising: the velocity dispersion of the tracers enters in equation (8) and thus directly affects the tracer density fall-off. By contrast, the mass-model velocity dispersion profiles appear only in equation (11) (through equation 9), and uncertainties in these profiles are marginalized out when we calculate $\rho_{\rm dm}$ and $\rho_{\rm s}$. Thus, it is vital to obtain an accurate determination of $\overline{v^2_{z,i}}(z)$ for our tracers, but not crucial to know the precise form of the mass model.

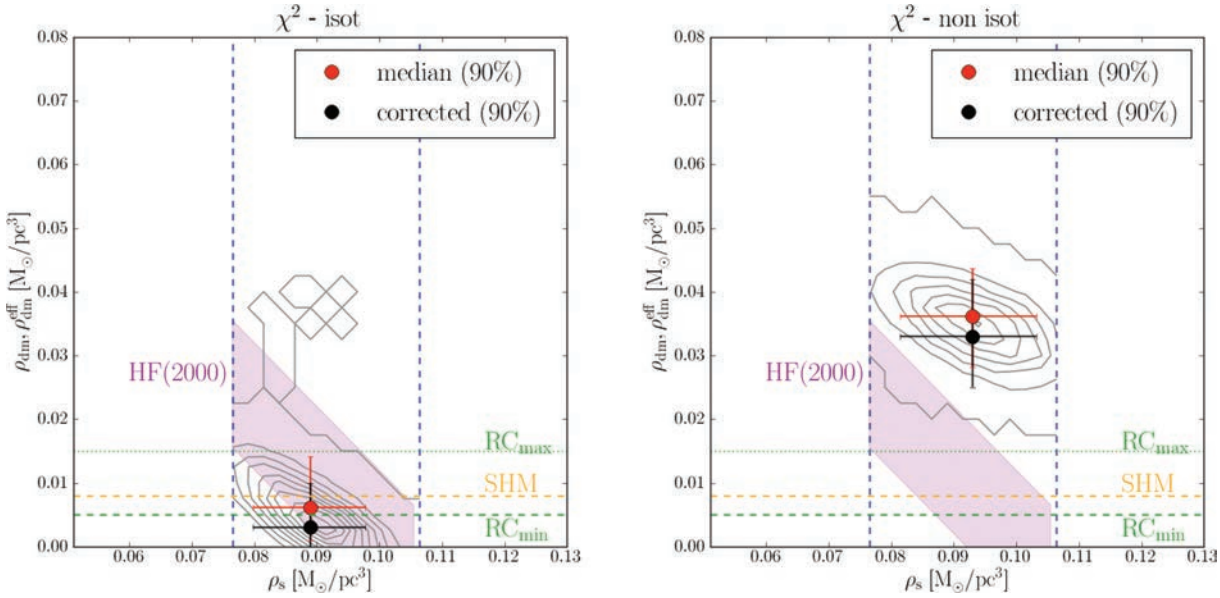

Figure 19. The recovered visible and dark matter densities calculated with the MA method, assuming isothermality (left-hand panel) and non-isothermality (right panel) of all the stellar populations for the real data. The grey contours represent the density of models explored by the MCMC and the red dot represents the median values of ρ_s and ρ_{dm}^{eff} (see equation 12); the red error bars correspond to the 90 per cent confidence interval of the distribution. The black dot is the result corrected for the rotation curve term calculated from the Oort constants (see Section 3.2.3). The purple area represents the values estimated by Holmberg & Flynn (2000). The blue-dashed lines show the imposed priors on ρ_s and ρ_{dm}. The green and yellow lines represent the minimum value and the maximum value of ρ_{dm} measured using rotation curves in the literature, and the SHM value, respectively.

Table 5. Extrapolated values of the local dark matter density using other methods from the literature. From these, we can place a reasonable lower limit on ρ_{dm} of $0.005\,M_\odot\,pc^{-3}$ ($\sim$0.20 GeV cm^{-3}).

$\rho_{dm}(R_\odot)$ (GeV cm^{-3})	Method	Reference
$0.519^{+0.021}_{-0.017}$	Microlensing+ mass modelling	Gates, Gyuk & Turner (1995)
0.385 ± 0.027	Bayesian approach + Einasto profile	Catena & Ullio (2010)
0.364	Rotation curve + spherical halo	Sofue et al. (2009)
0.20–0.52[a]	Rotation curve + mass modelling[b]	Weber & de Boer (2010)

[a]Range for the different mass models considered.
[b]This is a lower limit calculated by considering a smooth dark matter halo; substructures can only enhance the local density.

5 CONCLUSIONS

We have revisited systematic problems in determining the local matter densities from stellar motions. We used a high-resolution *N*-body simulation of a MW-like galaxy to test different methods in the literature and the systematic errors potentially introduced by their assumptions. We introduced a new method – the MA method – based on moments of the Jeans equations, combined with an MCMC technique to marginalize over the unknown parameters. Given sufficiently good data, we showed that our MA method can recover the correct local dark matter density even in the face of disc inhomogeneities, non-isothermal tracers and the non-separability of the *z*-motion. Finally, we illustrated the power of our approach by applying it to *Hipparcos* data from the literature.

Our key results are as follows:

(i) As noted previously by Bahcall (1984c), data up to high z ($|z| \sim 0.6$ kpc – i.e. significantly larger than the MW disc scale-height) are required to break the degeneracy between the local dark matter density, ρ_{dm}, and the local visible matter density, ρ_s.

(ii) Methods that assume that the distribution function of a tracer population is a function only of the vertical energy $f = f(E_z)$ become systematically biased if the motion of the tracers is not truly separable in z. This effect becomes important when fitting to data that extend to heights larger than the disc scaleheight – as is necessary to break the ρ_{dm}–ρ_s degeneracy [cf. point (i) above]. The initial conditions in our simulation were separable, but as the disc evolves and reaches a true equilibrium, the distribution function is no longer separable. If we assume that $f = f(E_z)$, then this introduces a systematic error that we have no way to correct. For this reason, we favour moment-based methods that assume nothing about the form of f.

(iii) We introduced a new MA method for recovering the local matter and dark matter densities, ρ_{tot} and ρ_{dm}, respectively. Our method is based on solving the combined Jeans–Poisson equations using an MCMC technique to marginalize over the unknown parameters. We showed that our MA method can correctly recover both ρ_{dm} and ρ_s even in the face of disc inhomogeneities, the non-separability of the z-motion and the vertical non-isothermality of the tracers, provided that the run of dispersion with height of the tracers, $\overline{v_{z,i}^2}(z)$, is known.

(iv) Our derived MA method is very sensitive to the precise form of $\overline{v_{z,i}^2}(z)$ for the tracers. For this reason, we interpolate the measured data (marginalizing out any velocity uncertainties), rather than assuming a functional form. By contrast, the form of $\overline{v_{z,i}^2}(z)$ for the other disc components in the mass model is not important; we may safely assume that these are isothermal.

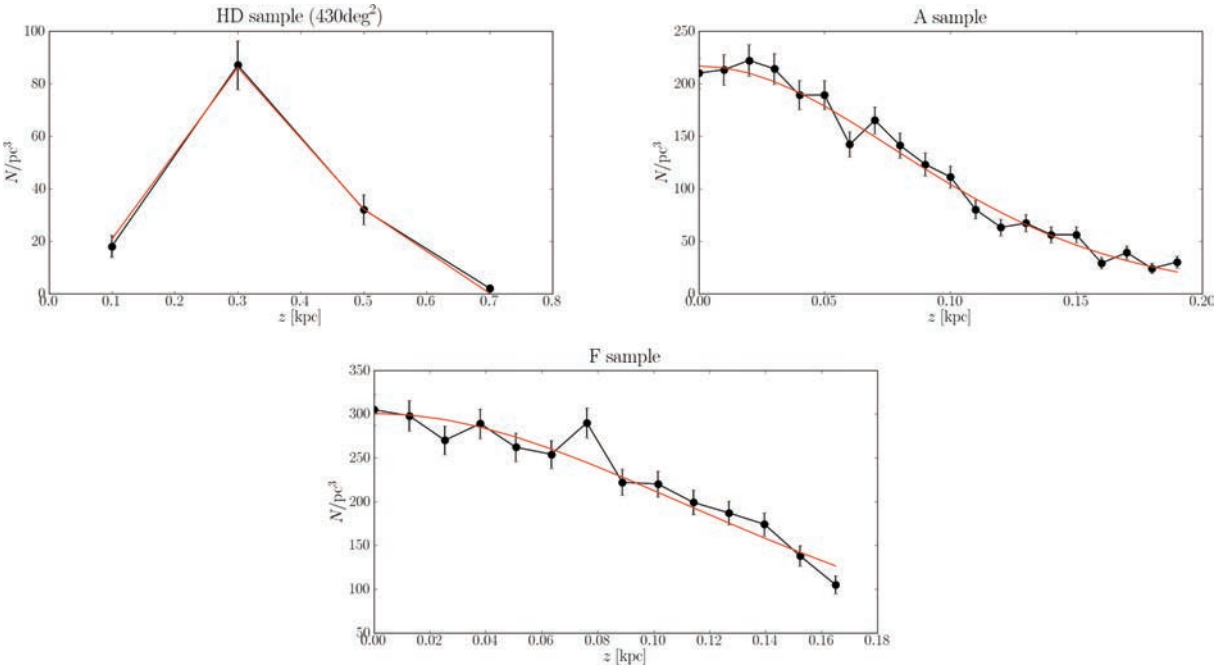

Figure 20. The recovered density fall-off for the three tracers considered, assuming isothermality of all the disc populations: the HD sample from Holmberg & Flynn (2004) (top left-hand panel); and the A- and F-star samples from Holmberg & Flynn (2000) (top right-hand and bottom panels). Similarly, good fits were obtained for the maximally non-isothermal model.

(v) We applied our new MA method to recent data from Holmberg & Flynn (2000, 2004). We first made the assumption that the star tracer populations (A, F, K stars) are isothermal. This recovered $\rho_{\rm dm} = 0.003^{+0.009}_{-0.007}\,{\rm M}_\odot\,{\rm pc}^{-3}$ (90 per cent confidence), consistent with previous determinations. If, however, we assume instead a non-isothermal profile similar to the blue disc stars from SDSS DR-7 (Abazajian et al. 2009) measured by Bond et al. (2010), we obtain a fit with a very similar χ^2 value, but with $\rho_{\rm dm} = 0.033^{+0.008}_{-0.009}\,{\rm M}_\odot\,{\rm pc}^{-3}$ (90 per cent confidence). This illustrates the importance of measuring $\overline{v^2_{z,i}}(z)$ for the tracers.

(vi) A combination of good statistics, precise knowledge of the local amount of visible matter and a good measure of $\overline{v^2_{z,i}}(z)$ for the tracers is crucial for obtaining an accurate unbiased measure of $\rho_{\rm tot}$ and $\rho_{\rm dm}$. This will become possible with future-generation Galactic surveys.

ACKNOWLEDGMENTS

We would like to thank Lawrence M. Widrow and John Dubinski for providing us with their latest version of the GALACTICS code and the parameters for the initial condition of our MW-like galaxy; Chris Flynn for giving us the *Hipparcos* data from Holmberg & Flynn (2004) and for many useful comments; and Hanni Lux for providing the structure of the MCMC code used in this work. JIR would like to acknowledge the support from SNF grant PP00P2_128540/1.

REFERENCES

Abazajian K. N. et al., 2009, ApJS, 182, 543
Aprile E., Giboni K. L., Majewski P., 2005, New Astron. Rev., 49, 289
Bahcall J. N., 1984a, ApJ, 276, 156
Bahcall J. N., 1984b, ApJ, 287, 926
Bahcall J. N., 1984c, ApJ, 276, 169
Bailer-Jones C. A. L., 2008, in Andersen J., Bland-Hawthorn J., Nordström B., eds, Proc. IAU Symp. 254, The Galaxy Disk in Cosmological Context. Cambridge Univ. Press, Cambridge, p. 475
Baudis L., 2006, Int. J. Mod. Phys. A, 21, 1925
Bienayme O., Robin A. C., Creze M., 1987, A&A, 180, 94
Binney J., Merrifield M., 1998, Galactic Astronomy. Princeton Univ. Press, Princeton, NJ
Binney J., Tremaine S., 2008, Galactic Dynamics, 2nd edn. Princeton Univ. Press, Princeton, NJ
Bond N. A. et al., 2010, ApJ, 716, 1
Branham R. L., Jr, 2010, MNRAS, 409, 1269
Catena R., Ullio P., 2010, J. Cosmol. Astropart. Phys., 8, 4
CDMS Collaboration, 2009, Phys. Rev. Lett., 102, 011301
Creze M., Chereul E., Bienayme O., Pichon C., 1998, A&A, 329, 920
Dehnen W., 2002, in Athanassoula E., Bosma A., Mujica R., eds, ASP Conf. Ser. Vol. 275, Disks of Galaxies: Kinematics, Dynamics and Peturbations. Astron. Soc. Pac., San Francisco, p. 105
Dehnen W., Binney J., 1998, MNRAS, 294, 429
Drimmel R., Spergel D. N., 2001, ApJ, 556, 181
Feast M., 2000, MNRAS, 313, 596
Flynn C., Freeman K. C., 1993, A&AS, 97, 835
Flynn C., Fuchs B., 1994, MNRAS, 270, 471
Flynn C., Holmberg J., Portinari L., Fuchs B., Jahreiß H., 2006, MNRAS, 372, 1149
Fuchs B., Wielen R., 1993, in Holt S. S., Verter F., eds, AIP Conf. Ser. Vol. 278, Back to the Galaxy. Am. Inst. Phys., New York, p. 580
Gaitskell R. J., 2004, Annu. Rev. Nucl. Part. Sci., 54, 315
Gates E., Gyuk G., Turner M., 1995, ApJ, 499, L123
Gingold R. A., Monaghan J. J., 1977, MNRAS, 181, 375
Guo Q., White S., Li C., Boylan-Kolchin M., 2010, MNRAS, 404, 1111
Holmberg J., Flynn C., 2000, MNRAS, 313, 209
Holmberg J., Flynn C., 2004, MNRAS, 352, 440
Jordan S., 2008, Astron. Nachr., 329, 875
Jungman G., Kamionkowski M., Griest K., 1996, Phys. Rep., 267, 195
Kuijken K., Gilmore G., 1989a, MNRAS, 239, 605
Kuijken K., Gilmore G., 1989b, MNRAS, 239, 651

Kuijken K., Gilmore G., 1989c, MNRAS, 239, 571
Kuijken K., Gilmore G., 1991, ApJ, 367, L9
Lacey C. G., Ostriker J. P., 1985, ApJ, 299, 633
Lake G., 1989, AJ, 98, 1554
Lucy L. B., 1977, AJ, 82, 1013
Maron J. L., Howes G. G., 2003, ApJ, 595, 564
Mignard F., 2000, A&A, 354, 522
Monaghan J. J., 1992, ARA&A, 30, 543
Ng Y. K., Bertelli G., Chiosi C., Bressan A., 1997, A&A, 324, 65
Ojha D. K., 2001, MNRAS, 322, 426
Oort J. H., 1932, Bull. Astron. Inst. Neth., 6, 249
Oort J. H., 1960, Bull. Astron. Inst. Neth., 15, 45
Pham H. A., 1997, in Perryman M. A. C., Bernacca P. L., eds, Hipparcos Venice '97, ESA SP-402. ESA, Noordwijk, p. 559
Read J. I., Lake G., Agertz O., Debattista V. P., 2008, MNRAS, 389, 1041
Read J. I., Mayer L., Brooks A. M., Governato F., Lake G., 2009, MNRAS, 397, 44
Saha P., 2003, Principles of Data Analysis. Cappella Archive, Great Malvern
Sánchez-Salcedo F. J., Flynn C., Hidalgo-Gámez A. M., 2011, ApJ, 731, L35
Seabroke G. M., Gilmore G., 2007, MNRAS, 380, 1348
Siebert A. et al., 2008, MNRAS, 391, 793
Smith M. C., Wyn Evans N., An J. H., 2009, ApJ, 698, 1110
Sofue Y., Honma M., Omodaka T., 2009, PASJ, 61, 227
Spagna A., Lattanzi M. G., Lasker B. M., McLean B. J., Massone G., Lanteri L., 1996, A&A, 311, 758
Stäckel 1895, C. R. Acad. Sci. Paris, 121, 489
Stadel J. G., 2001, PhD thesis, Univ. Washington
Statler T. S., 1989, ApJ, 344, 217
Steinmetz M., 2003, in Munari U., ed., ASP Conf. Proc. Vol. 298, GAIA Spectroscopy: Science and Technology. Astron. Soc. Pac., San Francisco, p. 381
Steinmetz M., Zwitter T., Siebert A., Watson F. G., Freeman K. C., Munari U., 2006, AJ, 132, 1645
Weber M., de Boer W., 2010, A&A, 509, 25
Widrow L. M., Dubinski J., 2005, ApJ, 631, 838
Widrow L. M., Pym B., Dubinski J., 2008, ApJ, 679, 1239
Xue X. X. et al., 2008, AJ, 684, 1143
Yanny B. et al., 2009, AJ, 137, 4377
Zwitter T. et al., 2008, AJ, 136, 421

APPENDIX A: INTRODUCTION OF DIMENSIONLESS VARIABLES

In Sections 2.1 and 2.2, we presented the basic equations used to calculate the potential in the MA and HF methods. In this appendix, we rewrite these equations (namely equations 8, 14 and 11) using dimensionless variables to simplify the calculations (Bahcall 1984a,b,c).

The Poisson equation (11) can be rewritten as

$$\frac{\partial^2\Phi}{\partial z^2} = 4\pi G\nu_{0,1}\left[\sum_{i=1}^{N}\frac{\nu_i(z)}{\nu_{0,1}} + \epsilon\right] \tag{A1}$$

with $\epsilon = \rho_{\rm dm}/\nu_{0,1}$ ($i = 1$ indicates the population with the largest scaleheight).

The following dimensionless variables can then be introduced:

$$\phi = \frac{\Phi}{\overline{v^2_{z,1}}}, \tag{A2}$$

$$z_1 = \sqrt{\frac{\overline{v^2_{z,1}}}{2\pi G\nu_{0,1}}}, \tag{A3}$$

$$x = \frac{z}{z_1}, \tag{A4}$$

$$\alpha_i = \frac{\overline{v^2_{z,1}}}{\overline{v^2_{z,i}}}, \tag{A5}$$

$$\xi_i = \frac{\nu_{0,i}}{\nu_{0,1}}, \tag{A6}$$

$$\epsilon = \frac{\rho_{\rm dm}}{\nu_{0,1}}, \tag{A7}$$

and the solution to equation (13) becomes

$$\nu_i(z) = \nu_{0,i}\exp[-\alpha_i\phi(z)]. \tag{A8}$$

Using this and the above dimensionless quantities, we can write

$$\frac{{\rm d}^2\phi}{{\rm d}x^2} = 2\sum_{i=1}^{N}\xi_i\exp(-\alpha_i\phi) + 2\epsilon \tag{A9}$$

with $\phi(0) = 0$ and ${\rm d}\phi(0)/{\rm d}x = 0$. For a specified ratio of the mass densities in the plane (ξ_i) to the velocity dispersions ($\alpha_i^{1/2}$), equation (A9) can then be integrated numerically for any ϵ.

Finally, for the MA method, we must define an additional dimensionless variable:

$$\alpha_{i,z} = \frac{\overline{v^2_{z,1}}(0)}{\overline{v^2_{z,i}}(z)}. \tag{A10}$$

In this way, we can write the solution to equations (13) and (11) as

$$\nu_i(z) = \xi_i\frac{\alpha_{i,z}}{\alpha_i}\exp\left(-\int_0^x\alpha_{i,z}\frac{{\rm d}\phi}{{\rm d}x}{\rm d}x\right), \tag{A11}$$

$$\frac{{\rm d}^2\phi}{{\rm d}x^2} = 2\left[\sum_{i=1}^{N}\xi_i\frac{\alpha_{i,z}}{\alpha_i}\exp\left(-\int_0^x\alpha_{i,z}\frac{{\rm d}\phi}{{\rm d}x}{\rm d}x\right) + \epsilon\right]. \tag{A12}$$

APPENDIX B: THE SPH ANALYSIS METHOD

The local density, velocity dispersion and derivatives for the Jeans equation terms are extracted from the simulation using weighted sums over the particles as in SPH (Gingold & Monaghan 1977; Lucy 1977; Monaghan 1992).

The density is given by

$$\nu_i = \sum_j^N m_j W(|\boldsymbol{r}_{ij}|, h_i), \tag{B1}$$

where h_i and m_j are the smoothing length and mass of particle i and j, respectively; we define $\boldsymbol{r}_{ij} = \boldsymbol{r}_i - \boldsymbol{r}_j$ and similarly for other vectors; W is a symmetric kernel that obeys the normalization condition

$$\int_V W(|\boldsymbol{r} - \boldsymbol{r}'|, h){\rm d}^3r' = 1 \tag{B2}$$

and the property

$$\lim_{h\to 0} W(|\boldsymbol{r} - \boldsymbol{r}'|, h) = \delta(|\boldsymbol{r} - \boldsymbol{r}'|). \tag{B3}$$

In the limit $N \to \infty$, $h \to 0$ (and using $m_j/\nu_j \to {\rm d}^3r'$), equation (B1) recovers the continuum density.

The smoothing lengths h_i were adapted to ensure a fixed enclosed mass $M_{\rm SPH} = mN_{\rm SPH}$, where m is the mass of a particle and $N_{\rm SPH} = 128$ is the neighbour number. We used the standard cubic spline smoothing kernel for W (Monaghan 1992).

The velocity dispersion tensor is given by

$$\sigma_{ab,i} = \frac{1}{\nu_i}\sum_j^N m_j v_{a,j} v_{b,j} W(|\boldsymbol{r}_{ij}|, h_i), \tag{B4}$$

where a, $b = [0, 1, 2]$ give the index of the velocity vector and velocity dispersion tensor, respectively.

Apart from the gradient of the gravitational potential that was taken directly from the tree (this is just the acceleration), gradients were calculated using a second-order accurate polynomial reconstruction at each point in the collisionless fluid, as in Maron & Howes (2003) and references therein. Briefly, assuming that the fluid is smooth (and therefore differentiable), we can perform a polynomial expansion at second order about a point i:

$$\begin{aligned} q_{ij} = {} & a_0 + a_1 x_{ij} + a_2 y_{ij} + a_3 z_{ij} + a_4 x_{ij}^2 + a_5 y_{ij}^2 + a_6 z_{ij}^2 \\ & + a_7 x_{ij} y_{ij} + a_8 x_{ij} z_{ij} + a_9 y_{ij} z_{ij} + O(h^3), \end{aligned} \tag{B5}$$

where $\boldsymbol{x}_{ij} = \boldsymbol{r}_{ij}/h_i = [x_{ij}, y_{ij}, z_{ij}]$ and q_i is the quantity we wish to differentiate at particle i (e.g. the density).

The coefficients of this expansion can then be determined by inverting the following 10×10 matrix equation:

$$\mathbf{M}\mathbf{a} = \mathbf{q}, \tag{B6}$$

where

$$\mathbf{a}^{\mathrm{T}} = [a_0, a_1, a_2, a_3, a_4, a_5, a_6, a_7, a_8, a_9], \tag{B7}$$

$$\mathbf{q}^{\mathrm{T}} = \sum_j^N m_j q_j \overline{W}_{ij}[1, x_{ij}, y_{ij}, z_{ij}, x_{ij}^2, y_{ij}^2, z_{ij}^2, x_{ij}y_{ij}, x_{ij}z_{ij}, y_{ij}z_{ij}], \tag{B8}$$

$$\mathbf{M} = \sum_j^N m_j \overline{W}_{ij} \begin{pmatrix} 1 & x_{ij} & y_{ij} \cdots \\ x_{ij} & x_{ij}^2 & x_{ij}y_{ij} \cdots \\ y_{ij} & y_{ij}x_{ij} & y_{ij}^2 \cdots \\ z_{ij} & z_{ij}x_{ij} & z_{ij}y_{ij} \cdots \\ x_{ij}^2 & x_{ij}^3 & x_{ij}^2 y_{ij} \cdots \\ y_{ij}^2 & y_{ij}^2 x_{ij} & y_{ij}^3 \cdots \\ z_{ij}^2 & z_{ij}^2 x_{ij} & z_{ij}^2 y_{ij} \cdots \\ x_{ij}y_{ij} & x_{ij}^2 y_{ij} & x_{ij}y_{ij}^2 \cdots \\ x_{ij}z_{ij} & z_{ij}x_{ij}^2 & x_{ij}z_{ij}y_{ij} \cdots \\ y_{ij}z_{ij} & y_{ij}z_{ij}x_{ij} & z_{ij}y_{ij}^2 \cdots \end{pmatrix}$$

$$\begin{pmatrix} \cdots z_{ij} & x_{ij}^2 & y_{ij}^2 & z_{ij}^2 \cdots \\ \cdots x_{ij}z_{ij} & x_{ij}^3 & x_{ij}y_{ij}^2 & x_{ij}z_{ij}^2 \cdots \\ \cdots y_{ij}z_{ij} & y_{ij}x_{ij}^2 & y_{ij}^3 & y_{ij}z_{ij}^2 \cdots \\ \cdots z_{ij}^2 & z_{ij}x_{ij}^2 & z_{ij}y_{ij}^2 & z_{ij}^3 \cdots \\ \cdots x_{ij}^2 z_{ij} & x_{ij}^4 & x_{ij}^2 y_{ij}^2 & x_{ij}^2 z_{ij}^2 \cdots \\ \cdots y_{ij}^2 z_{ij} & y_{ij}^2 x_{ij}^2 & y_{ij}^4 & y_{ij}^2 z_{ij}^2 \cdots \\ \cdots z_{ij}^3 & z_{ij}^2 x_{ij}^2 & z_{ij}^2 y_{ij}^2 & z_{ij}^4 \cdots \\ \cdots x_{ij}y_{ij}z_{ij} & y_{ij}x_{ij}^3 & x_{ij}y_{ij}^3 & x_{ij}y_{ij}z_{ij}^2 \cdots \\ \cdots x_{ij}z_{ij}^2 & z_{ij}x_{ij}^3 & x_{ij}z_{ij}y_{ij}^2 & x_{ij}z_{ij}^3 \cdots \\ \cdots y_{ij}z_{ij}^2 & y_{ij}z_{ij}x_{ij}^2 & z_{ij}y_{ij}^3 & y_{ij}z_{ij}^3 \cdots \end{pmatrix}$$

$$\begin{pmatrix} \cdots x_{ij}y_{ij} & x_{ij}z_{ij} & y_{ij}z_{ij} \\ \cdots x_{ij}^2 y_{ij} & x_{ij}^2 z_{ij} & x_{ij}y_{ij}z_{ij} \\ \cdots x_{ij}y_{ij}^2 & y_{ij}x_{ij}z_{ij} & y_{ij}^2 z_{ij} \\ \cdots z_{ij}x_{ij}y_{ij} & x_{ij}z_{ij}^2 & y_{ij}z_{ij}^2 \\ \cdots x_{ij}^3 y_{ij} & x_{ij}^3 z_{ij} & x_{ij}^2 y_{ij}z_{ij} \\ \cdots x_{ij}y_{ij}^3 & y_{ij}^2 x_{ij}z_{ij} & y_{ij}^3 z_{ij} \\ \cdots z_{ij}^2 x_{ij}y_{ij} & x_{ij}z_{ij}^3 & y_{ij}z_{ij}^3 \\ \cdots x_{ij}^2 y_{ij}^2 & y_{ij}x_{ij}^2 z_{ij} & x_{ij}y_{ij}^2 z_{ij} \\ \cdots z_{ij}x_{ij}^2 y_{ij} & x_{ij}^2 z_{ij}^2 & x_{ij}y_{ij}z_{ij}^2 \\ \cdots z_{ij}x_{ij}y_{ij}^2 & y_{ij}x_{ij}z_{ij}^2 & y_{ij}^2 z_{ij}^2 \end{pmatrix} \tag{B9}$$

and $\overline{W}_{ij} = \frac{1}{2}[W_{ij}(h_i) + W_{ij}(h_j)]$ is the symmetrized smoothing kernel (the superscript $^{\mathrm{T}}$ means transpose).

Having determined all of the coefficients of $\mathbf{a}$ (by solving $\mathbf{a} = \mathbf{M}^{-1}\mathbf{q}$), the gradients of $\mathbf{q}$ evaluated at i then simply follow as

$$\frac{\partial q_i}{\partial x} = a_1; \frac{\partial q_i}{\partial y} = a_2; \frac{\partial q_i}{\partial z} = a_3. \tag{B10}$$

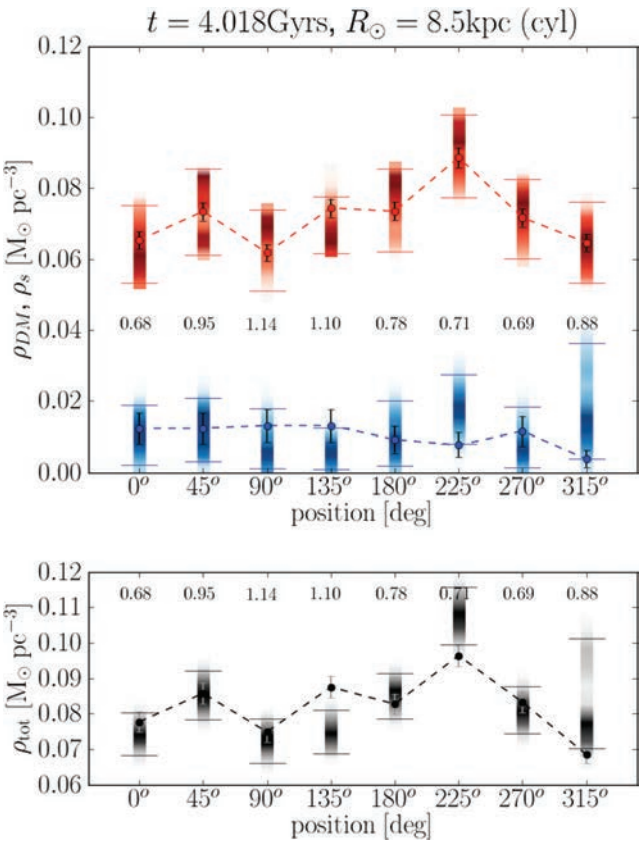

Figure C1. Models explored by the MCMC for the MA method for eight cylindrical 'solar neighbourhood' volumes applied to the evolved simulation at $R = 8.5$ kpc. Upper panel: recovered values of the dark and visible matter densities. Lower panel: recovered values of the total (dark+visible) matter density. The symbols and colours are as in Fig. 15.

APPENDIX C: RESULTS FOR THE EVOLVED SIMULATION (CYLINDERS)

In Section 3.3.2, we applied the HF and MA methods to the evolved simulation, considering several wedge-shaped volumes at a Galactocentic distance $R = 8.5$ kpc around the disc. These wedge-shaped volumes allowed us to sample the star particles sufficiently well that we could study systematic errors on the recovery of the local density, without being affected by sampling errors.

In this appendix, we consider also the effects of sample error on the evolved simulation. We show the results for smaller cylindrical volumes at $R = 8.5$ kpc identical to those used to study the unevolved simulation in Section 3.3.1. These volumes have a sampling and a shape similar to the *Hipparcos* data analysed by Holmberg & Flynn (2000) ($\sim$2000–3000 within $|z| < 200$ pc). In Fig. C1, we show the results for the MA method using cylindrical volumes. Now, due to the smaller volume sampled, the velocity dispersion $\overline{v_z^2}(z)$ is quite noisy. To deal with this problem, we use the MCMC to marginalize over the velocity errors. At each iteration at the MCMC, we draw a value of $\overline{v_z^2}(z)$ for each z bin. We assume a Gaussian error distribution with a width corresponding to the uncertainty on $\overline{v_z^2}(z)$. (Note that this approach is readily adapted to real data where $\overline{v_z^2}(z)$ is also likely to be noisy and uncertain.) As can be seen in Fig. C1, we can recover the correct value of the local visible, dark matter and total densities inside the errors for most of the volumes. Because of the poorer sampling, the uncertainties on the local density values are larger than those obtained with the wedges (see Fig. 16).

This paper has been typeset from a TEX/LATEX file prepared by the author.